ADVANCED FUNCTIONAL MATERIALS
www.afm-journal.de

Advances in Advanced In Situ Assembled Composite Electrode Materials for Enhanced Solid Oxide Cell Performance

Yufei Song, Yixiao Song, Yuhao Wang, Yunfeng Tian, Jingwei Li, Meigui Xu, Zongping Shao, and Francesco Ciucci**

Solid oxide cells (SOCs) hold considerable promise as devices for efficient, reversible conversion between chemical and electrical energy, facilitating a global shift toward renewable energy. Electrode performance is critical for SOC efficiency and durability and composite materials are key to developing high-performance electrode catalysts. However, conventional mechanical mixing and infiltration methods often lead to large particle sizes, uneven distribution, and weak interfacial interactions, thus limiting electrochemical activity and longevity. Recent advancements have produced powerful new strategies for creating composite materials. These include metal exsolution and oxide segregation for fuel electrodes and one-pot synthesis, segregation, phase reaction, and dynamic cation exchange for air electrodes. These techniques yield highly active, uniform nano-catalysts and robust multi–*p*hase interfacial contacts, significantly improving electrochemical activity and durability. This work reviews these advanced strategies and their applications in SOCs. It provides valuable insights for designing and optimizing SOC catalyst materials, accelerating the development of this vital energy conversion technology.

1. Introduction

Solid oxide cells (SOCs) represent a breakthrough in energy storage and conversion technology. These versatile devices can convert various fuels, such as hydrogen, natural gas, methane, and ethanol, directly into electricity. Unlike traditional combustion-based power systems,[1] SOCs achieve remarkable efficiency with significantly reduced emissions. In electrolysis mode, SOCs go even further: they use renewable energy to produce sustainable fuels like hydrogen and ammonia. For example, this involves converting water and carbon dioxide into value-added fuels such as H_2, syngas, ethylene, and so on.[2] This adaptability makes SOCs a pivotal technology for both the energy and chemical industries.

The performance of SOCs depends strongly on the electrochemical properties and longevity of their electrodes. These electrodes must electro-catalyze many complex reactions, including oxygen reduction and evolution at the air electrode and fuel oxidation and formation at the fuel electrode.[3–5] Ideal electrodes require efficient adsorption and desorption of reactants, excellent ionic and electronic conductivity, and electrochemical and thermochemical stability.[6,7] Single-phase materials often struggle to meet all these demands. For instance, Ni metals, commonly used in SOC fuel electrode catalysts, are known for their

Y. Song, Y. Wang, F. Ciucci
Department of Mechanical and Aerospace Engineering
The Hong Kong University of Science and Technology
Clear Water Bay, Hong Kong SAR 999077, P. R. China
E-mail: francesco.ciucci@uni-bayreuth.de

Y. Song, M. Xu, Z. Shao
State Key Laboratory of Materials-Oriented Chemical Engineering
College of Chemical Engineering
Nanjing Tech University
Nanjing 210009, China
E-mail: shaozp@njtech.edu.cn

The ORCID identification number(s) for the author(s) of this article can be found under https://doi.org/10.1002/adfm.202405851

DOI: 10.1002/adfm.202405851

J. Li, F. Ciucci
Chair of Electrode Design for Electrochemical Energy Storage Systems
University of Bayreuth
95448 Bayreuth, Bavaria, Germany

Z. Shao
WA School of Mines: Minerals
Energy and Chemical Engineering (WASM-MECE)
Curtin University
Perth, WA 6845, Australia

Y. Tian
China University of Mining and Technology
Xu Zhou 221116, China

J. Li, F. Ciucci
Bavarian Center for Battery Technology (BayBatt)
University of Bayreuth
Universitätsstraße 30, 95447 Bayreuth, Bavaria, Germany

catalytic activity and electronic conductivity.[6,8] However, if Ni metal is directly used as a fuel electrode, restricted ionic transport in the fuel electrode restricts reaction to the triple-phase boundary. Similarly, $La_{0.8}Sr_{0.2}MnO_3$, a conventional single-phase perovskite air electrode material, lacks ionic conductivity and thus also limits active sites.[9,10] While advanced materials like $BaCo_{0.4}Fe_{0.4}Zr_{0.1}Y_{0.1}O_{3-\delta}$[11] and $PrBa_{0.5}Sr_{0.5}Co_{1.5}Fe_{0.5}O_{5+\delta}$,[12] offer mixed ionic conductivity for superior performance, their phase instability and thermal incompatibility with the electrolyte can hinder long-term stability.

Composite materials offer a compelling solution to the limitations of single-phase electrodes, combining desired properties such as enhanced ion transport and thermal compatibility. For instance, compositing Ni or $La_{0.8}Sr_{0.2}MnO_3$ with oxygen ion conductors like yttria-stabilized zirconia (YSZ),[13,14] $Sm_{0.2}Ce_{0.8}O_{1.9}$ (SDC),[15,16] or proton conductors like Ba(Zr,Ce)O_3-based materials,[17,18] extends active sites beyond the electrode/electrolyte interface by improving ion transport. Similarly, blending low thermal expansion materials with $BaCo_{0.4}Fe_{0.4}Zr_{0.1}Y_{0.1}O_{3-\delta}$ or $PrBa_{0.5}Sr_{0.5}Co_{1.5}Fe_{0.5}O_{5+\delta}$,[19,20] can improve thermal compatibility between electrode and electrolyte components.

However, conventional methods like mechanical mixing and infiltration present certain drawbacks.[16,21] Mechanical mixing often leads to uneven phase distribution, large catalyst particles, and weak inter-phase contact. This threatens long-term SOC performance due to sintering and phase separation of the catalysts.[22] Infiltration, while allowing for the production of nanocomposites, often results in nanoparticles that are poorly anchored to their support, in turn increasing their tendency to aggregate over time.[23]

In situ assembled composite materials offer a solution to the limitations of conventional composite preparation techniques. These composites form spontaneously either during synthesis or under SOC operating conditions. Due to the high-temperature reducing the environment of fuel electrodes, in situ assembly can be driven by mechanisms such as metal exsolution[24,25] and oxide segregation.[26] Air electrodes also benefit from in situ assembly techniques, including one-pot synthesis,[27] segregation,[28,29] phase reaction,[30] and dynamic cation exchange.[31] In situ assembly offers several advantages relative to conventional methods, such as mechanical mixing and infiltration. This approach blends the unique functionalities of each phase to create composite electrodes that simultaneously address the multiple needs of SOCs, including high catalytic activity, electronic-ionic conductivity, thermal compatibility, and chemical stability. In situ assembly often yields nanocomposites with uniform phase distribution and strong nanoscale contact, maximizing catalytic centers. Additionally, phase interdiffusion within these composites results in robust chemical adhesion, preventing nano-catalyst sintering. Despite the transformative potential of these strategies, a comprehensive overview of advanced in situ assembly techniques within the SOC field is still lacking.

This review systematically evaluates recent advances in in situ assembly strategies for SOC electrodes. We highlight material design techniques, including metal exsolution and oxide segregation for fuel electrodes, as well as one-pot synthesis, segregation, phase reaction, and dynamic cation exchange for air electrodes. Additionally, we consider current challenges and offer an outlook for this evolving field. This article also aims to guide the development of in situ assembled composite catalysts, driving innovation in energy storage and conversion technologies.

2. Introduction to SOCs

SOCs can be broadly categorized as oxygen- (O-SOCs) and proton-based (H-SOCs) cells, depending on the type of electrolyte used (**Figure 1a,b**).[1,2,7,32–35] Conventional O-SOCs, which use oxygen conductor YSZ, typically operate at temperatures ranging from 800–1000 °C.[13,14,36–39] At such high temperatures, O-SOCs usually suffer performance degradation caused by corrosion, phase transition of components, phase reaction, and thermally induced mechanical incompatibility among components.[40] In addition, operating O-SOCs at 800–1000 °C increases sealing and interconnection costs, hindering commercialization.[41] In recent decades, significant efforts have been directed toward developing electrolyte materials with high ionic conductivity and novel fabrication methods for thin-film electrolytes.[7,42–44] CeO_2-based electrolyte materials, such as SDC and $Gd_{0.2}Ce_{0.8}O_{1.9}$, have been found to exhibit higher oxygen-ion conductivity at intermediate temperature ranges when compared to YSZ.[37,42,45–47] Consequently, O-SOCs that employ these oxygen-ion-conducting electrolytes can operate in the temperature range of 450–600 °C.[46,48–50]

Relative to O-SOCs, current leading proton electrolytes, such as $BaZr_{0.8}Y_{0.2}O_{3-\delta}$,[18,51] $BaZr_{0.4}Ce_{0.4}Y_{0.2}O_{3-\delta}$,[52] $BaZr_{0.1}Ce_{0.7}Y_{0.1}Yb_{0.1}O_{3-\delta}$ (BZCYYb),[11,52–54] and $BaZr_{0.4}Ce_{0.4}Y_{0.1}Yb_{0.1}O_{3-\delta}$,[12,55,56] can be used to reduce operating temperatures to 350–550 °C. Various thin-film electrolyte fabrication techniques, including chemical vapor deposition,[57] atomic layer deposition,[58] pulsed laser deposition,[59] and physical vapor deposition,[60] have been successfully deployed to minimize ohmic losses. However, limited electrode electrochemical activity at lower operating temperatures presents a major challenge for H-SOCs. Therefore, developing new electrode materials with reduced polarization losses in this temperature range is critical.

In SOCs, the fuel electrode is the key component catalyzing fuel oxidization and formation reactions.[61] Ideally, an electrode handles a diverse range of fuels, including H_2,[62–66] NH_3,[64,67–69] hydrocarbon (C_xH_y),[33,56,70,71] CO,[63,66,72] syngas,[66,73–75] and natural gas (Figure 1).[76–78] To achieve high performance and efficiency, the fuel electrode must fulfill several key requirements. First, it must exhibit outstanding catalytic activity to efficiently break and form chemical bonds (such as H—H, N—H, and C—H). Secondly, mixed conductivity (for both electronic and ionic transport) is vital. Additionally, the electrode should have a large electrocatalytically active surface area, maximizing available reaction sites. Resistance to impurities, such as sulfur and carbon deposits from the use of hydrocarbon fuels, is also essential, alongside anti-sintering properties and thermomechanical compatibility with the electrolyte to ensure long-term durability.[6,76,79,80]

Conventional fuel electrodes consist of Ni-based cermet, such as Ni-YSZ, Ni-SDC, and Ni—$Gd_{0.2}Ce_{0.8}O_{1.9}$ for oxygen-ion conducting O-SOCs,[13,81–83] and Ni—Ba(Zr,Ce)$O_{3-\delta}$-based materials for proton-conducting H-SOCs.[84,85] Ni metal is an effective fuel electrode due to its cost-effectiveness, high activity, high

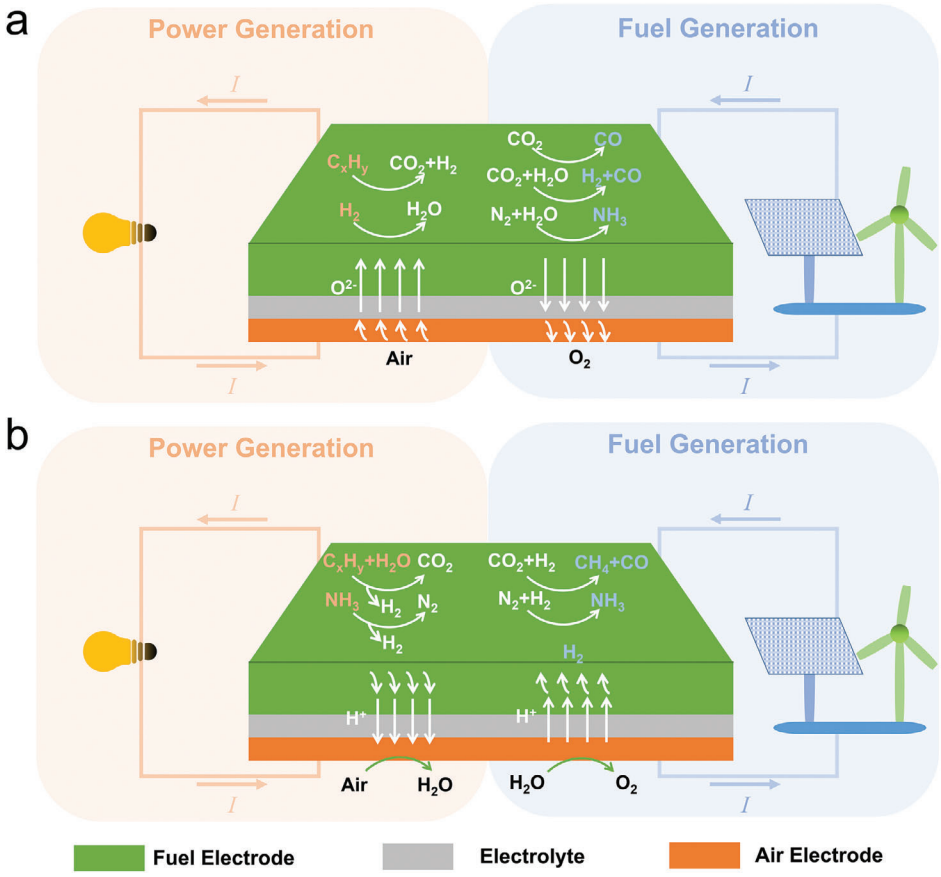

Figure 1. Schematics of a) O-SOC and b) H-SOC for power and fuel production.

electronic conductivity, thermal expansion coefficient (12–14 $\times 10^{-6}$ K^{-1})[86] matching SOC electrolytes (e.g., 12.4 $\times 10^{-6}$, 10.4 $\times 10^{-6}$, and 10.8 $\times 10^{-6}$ K^{-1} for SDC,[26] YSZ,[87] and BZCYYb,[88] respectively) and excellent redox stability.[13,89,90] Despite these advantages, conventional mechanically mixed Ni-based cermet suffer from several drawbacks, including the uneven dispersion of Ni particles,[91] poor anchoring between Ni catalyst and ionic conductors, leading to agglomeration during operation,[22,92–94] and poor resistance to sulfur poisoning and coking.[89,95–104] Mixed ion-electron conducting materials have been used as fuel electrodes because they can extend the electrocatalytically active surface areas, thereby reducing polarization resistances.[105–108] Perovskites, which are prototypical mixed ion-electron conducting materials, have also been studied as fuel electrodes.[109,110] Titanates and chromites are conventional perovskite fuel electrode materials, offering stability under high temperatures, reduced atmospheres, as well as excellent coke/sulfur resistance.[111–118] However, the catalytic activity of these materials toward fuel oxidation is inherently low, making modifications with active metal catalysts, such as Ni, Co, and Fe,[22,92,119] a necessary approach to enhance the performance of SOCs.

SOC air electrodes must be electrocatalytically active toward oxygen evolution/reduction reactions (OER/ORR) (Figure 1).[120,121] Mixed ion-electron transport capability is essential to expand the active area for electrocatalysis, thereby enhancing performance.[27,122–124] Perovskite materials are often used for this purpose.[125–127] However, purely electronic conductors like $La_{0.8}Sr_{0.2}MnO_3$ have activity confined to the region where the electrolyte, electrode, and gas phase meet, which leads to suboptimal performance.[14,128–130] Recently, Co- and Fe-based perovskites have gained popularity due to their high reducibility and ability to create oxygen vacancies, thus improving the conductivity of oxygen ions.[125,131–134] $La_{0.6}Sr_{0.4}CoO_{3-\delta}$,[135] $La_{0.6}Sr_{0.4}Co_{0.2}Fe_{0.8}O_{3-\delta}$,[136–138] and $Ba_{0.5}Sr_{0.5}Co_{0.8}Fe_{0.2}O_{3-\delta}$,[139] for instance, are effective O-SOC air electrodes due to their mixed O^{2-}/e^- conductivity. For H-SOCs, proton conductivity is also necessary to expand the active site region to the entire electrode surface.[140] Prominent H-SOC air electrode materials, such as $BaCo_{0.4}Fe_{0.4}Zr_{0.1}Y_{0.1}O_{3-\delta}$[11] and $PrBa_{0.5}Sr_{0.5}Co_{1.5}Fe_{0.5}O_{5+\delta}$,[12] perform well but face challenges such as thermal incompatibility with electrolytes and structural instability under high-temperature dry or humidified air conditions.

3. Strategies for Composite Electrode Materials

3.1. Conventional Methods

3.1.1. Mechanical Mixing

Mechanical mixing is a commonly used physical method for combining (e.g., through ball milling) powders of multiple

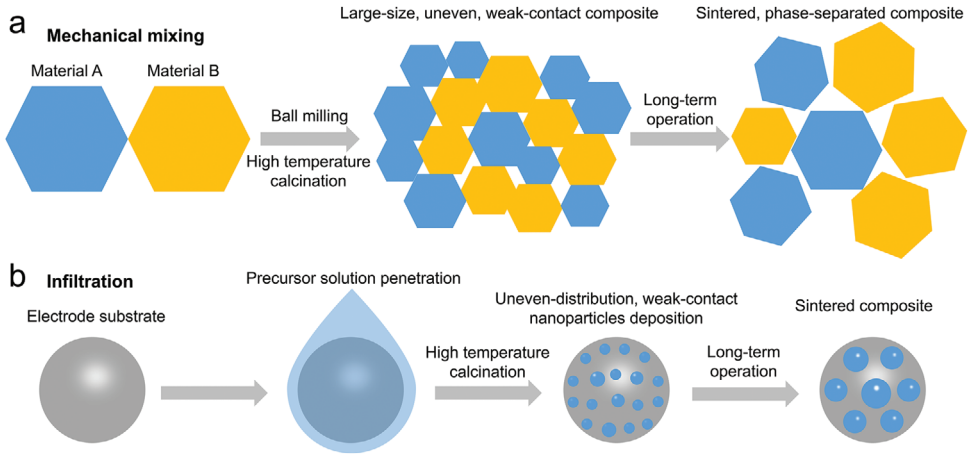

Figure 2. Schematic illustration of conventional SOC electrode fabrication methods: a) mechanical mixing and b) infiltration.

materials (**Figure 2a**). This technique is conventionally used to produce composite fuel (e.g., Ni-YSZ,[37,98] Ni-SDC,[141] Ni-BZCYYb),[34,142] and air (e.g., $La_{0.8}Sr_{0.2}MnO_3$-YSZ,[143] $Ba_{0.5}Sr_{0.5}Co_{0.8}Fe_{0.2}O_{3-\delta}$-SDC,[144] and $Ba_{0.5}Sr_{0.5}Co_{0.8}Fe_{0.2}O_{3-\delta}$-BZCYYb),[145] electrode materials. Despite the popularity of this method, mechanically mixed composites suffer drawbacks such as large particle size, uneven distribution, and weak contact between phases. These limitations reduce the availability of active sites, and under the demanding long-term operating conditions of SOCs, can lead to sintering, phase separation, and ultimately, compromised performance and stability (Figure 2a).

3.1.2. Infiltration

Infiltration involves impregnating a porous electrode with a precursor solution and then calcining it at high temperatures to form the desired material within the electrode (Figure 2b). This method has produced fuel electrode materials (e.g., Ni-infiltrated YSZ,[146] BZCYYb-infiltrated Ni-YSZ,[147] and air electrode materials (e.g., $Sm_{0.5}Sr_{0.5}CoO_{3-\delta}$-infiltrated $La_{0.6}Sr_{0.4}Co_{0.2}Fe_{0.8}O_{3-\delta}$,[148] $BaCo_{0.4}Fe_{0.4}Zr_{0.1}Y_{0.1}O_{3-\delta}$-infiltrated BZCYYb).[11] Infiltrated catalysts often feature smaller, more uniformly distributed nanoparticles for improved activity compared to mechanically mixed materials. While impregnated materials are usually chosen so that they do not react with the substrate during calcination or SOC operation, infiltration with reactive materials, such as SrO,[149] and BaO,[29] leads to in situ composite assembly. Furthermore, infiltration still faces challenges, including uneven distribution, weak contact with the substrate, and susceptibility to sintering and poisoning within the harsh SOC operating environment (Figure 2b). Additionally, the infiltration process itself can be complex and time-consuming.[16]

3.2. In situ Assembly Methods

In situ assembly describes the spontaneous formation of composites during either materials synthesis or SOC operation. In this process, one phase lattice grows within or from another, promoting natural interdiffusion between multiple phases. The in situ assembly method often yields nanocomposites with exceptionally strong adhesion between phases. Compared to conventional methods, such as mechanical mixing and infiltration, nanocomposites produced by in situ assembly frequently exhibit smaller catalyst sizes, more uniform distribution, and improved interfacial contact. Those are all factors that directly contribute to enhanced activity and long-term stability.[31,52]

3.2.1. In situ assembly Strategies for Fuel Electrode

In situ assembly strategies, primarily metal exsolution and oxide segregation, can be used to prepare high-performance composite fuel electrodes for SOCs.[24–26,150] Metal exsolution proceeds in four steps: cation diffusion, cation reduction, nanoparticle nucleation, and nanoparticle growth. First, metal cations move from the material's interior to the surface, where they undergo reduction to metallic form.[150–153] These reduced metal atoms cluster into nanoparticles that expand over time. Oxide segregation, which is often triggered by metal exsolution or phase transitions, is less understood due to the challenges inherent in its characterization. **Figure 3** presents schematically the exsolution techniques used for in situ assembly of composite fuel electrodes. Figure 3a illustrates the process of B-site metal exsolution in a perovskite. The perovskite structure relies on its BO_6 octahedra for stability. When the B-site contains readily reducible cations (such as Fe, Co, Ni), their exsolution can destabilize the structure, triggering a collapse and phase decomposition of the starting material. As exsolving cations induce reduction and subsequent lattice distortion, this process can result in the formation of a Ruddlesden-Popper-type $A_{n+1}B_nO_{3n+1}$ perovskite (Figure 3a).[154,155] Conversely, when the B-site is rich in high-valence, less-reducible elements (e.g., Zr, Ce, Y, Cr, Ti),[26,34] the exsolution of B-site cations favors the exsolution of A-site cations as oxides (Figure 3b). These cations with fixed valence resist lattice distortions, thereby preventing phase transitions and preserving the ABO_3 structure.[26] Kim and coworkers demonstrated that the transition from a single perovskite to an A-site ordered double perovskite can also

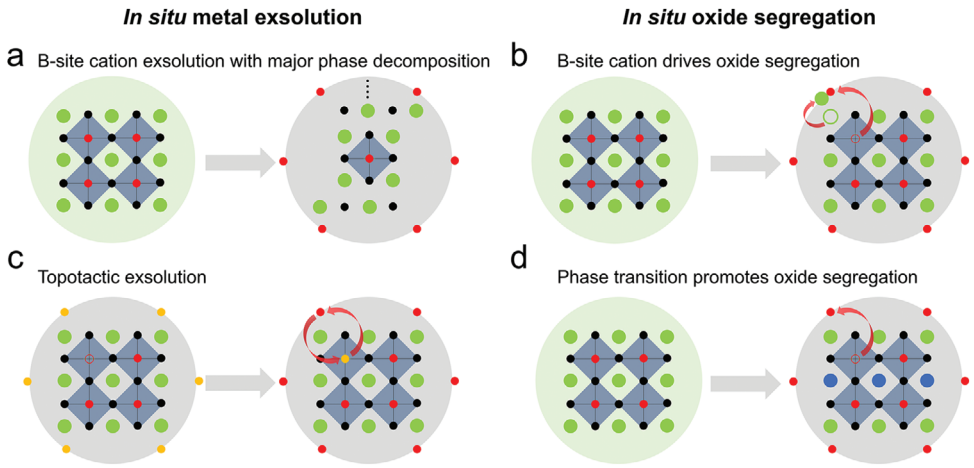

Figure 3. Potential in situ assembly processes of SOC electrodes, including a) B-site cation exsolution and major phase transition, b) B-site cation exsolution with subsequent oxide segregation, c) topotactic exsolution, and d) phase-transition-induced oxide segregation.

induce the segregation of B-site cations as oxides. Specifically, they transformed a single-perovskite material $Nd_{0.5}Ba_{0.5}MnO_3$ to A-site ordered layer $NaBaMn_2O_{5+\delta}$ by treating the $Nd_{0.5}Ba_{0.5}MnO_3$ powder at 800 °C under H_2; due to this phase transformation, metal Mn enriches the perovskite surface as an oxide (Figure 3d).[156]

As outlined above, conventional exsolution can lead to structural instability due to the removal of B-site cations. Topotactic exsolution offers a strategy to prevent this issue through a cationic swap. In this method, a metal is deposited onto a base material, triggering a cation exchange. Ideally, this swap replaces cations within the starting oxide phase with the deposited metal (Figure 3c). The deposited metal ions integrate into the oxide, simultaneously displacing existing oxide cations to the surface. This process forms nanoparticles without creating B-site vacancies, thus maintaining the stability of the host phase. Notably, topotactic ion exchange can also facilitate bulk cation exsolution, though to a lesser degree than conventional exsolution, which increases the number of active sites.[25]

3.2.2. In situ Assembly Strategies for Air Electrode Materials

In situ assembly strategies offer powerful routes for tailoring the properties of air electrode materials. Key methods include one-pot synthesis, enabling direct control over composition and nanostructure;[27] phase segregation, leading to the formation and separation of distinct active phases (e.g., metal, oxide, etc.);[28,29] phase reaction, facilitating the creation of novel composite materials;[30] dynamic cationic exchange, which fine-tunes material properties through cation redistribution.[31] **Figure 4** schematically illustrates these methods.

One-pot synthesis offers a significant improvement over mechanical mixing, overcoming drawbacks such as large particle size, uneven distribution, and poor interfacial contact.[157] This method involves conventional preparation steps (dissolving nitrates, drying, calcination) but with precise and unique parameter control. The result is the formation of nanoscale, uniformly distributed multi–*p*hase materials (Figure 4a).[31,52] Furthermore, the atomic-level mixing and nanoscale interfaces inherent in one-pot synthesis promote cation exchange.[157] By carefully adjusting calcination conditions, this method allows for tailored material properties, directly enhancing electrode performance.

Air electrodes often suffer from slow surface reaction kinetics, limiting their electrocatalytic activity toward oxygen reduction. While conventional infiltration methods attempt to address this by loading nano-catalysts (e.g., CeO_2,[158] Co_3O_4),[159] onto the electrode surface, weak interfacial contact leads to sintering and separation of these catalysts during SOC operation. In situ assembly of surface nano-catalysts through phase segregation offers a powerful solution to this issue. This process typically involves introducing specific mediators (e.g., H_2/O_2,[160,161] water vapor,[46] CO_2,[162] and oxides, including BaO,[29] SrO)[149] to the material's surface. These mediators trigger cation segregation, leading to surface enrichment or the formation of new, surface-bound catalysts (Figure 4b). In situ-grown nano-catalysts exhibit large active areas and strong adhesion to the main phases, enhancing activity and resisting sintering for enhanced stability.

The term "phase reaction" describes the interaction between two or more pre-existing materials under specific conditions (e.g., high-temperature calcination). This can lead to cation exchange and the formation of new phases.[30] These phase reactions commonly occur within air electrodes or at the electrode|electrolyte interface (Figure 4c). Reaction conditions, such as calcination temperature and duration, significantly influence phase reactions. By controlling these parameters, SOC performance can be enhanced.

Dynamic cation exchange is a less common approach for improving the performance of air electrodes. This approach leverages a single cation being shared among distinct phases within a composite material, which is synthesized in a one-pot process. This cation undergoes redistribution between the phases during operation at elevated SOC temperatures. This dynamic exchange is driven by the changing chemical environment within the material as it transitions between multiple stable phases. The redistribution alters the composition and relative proportions of these

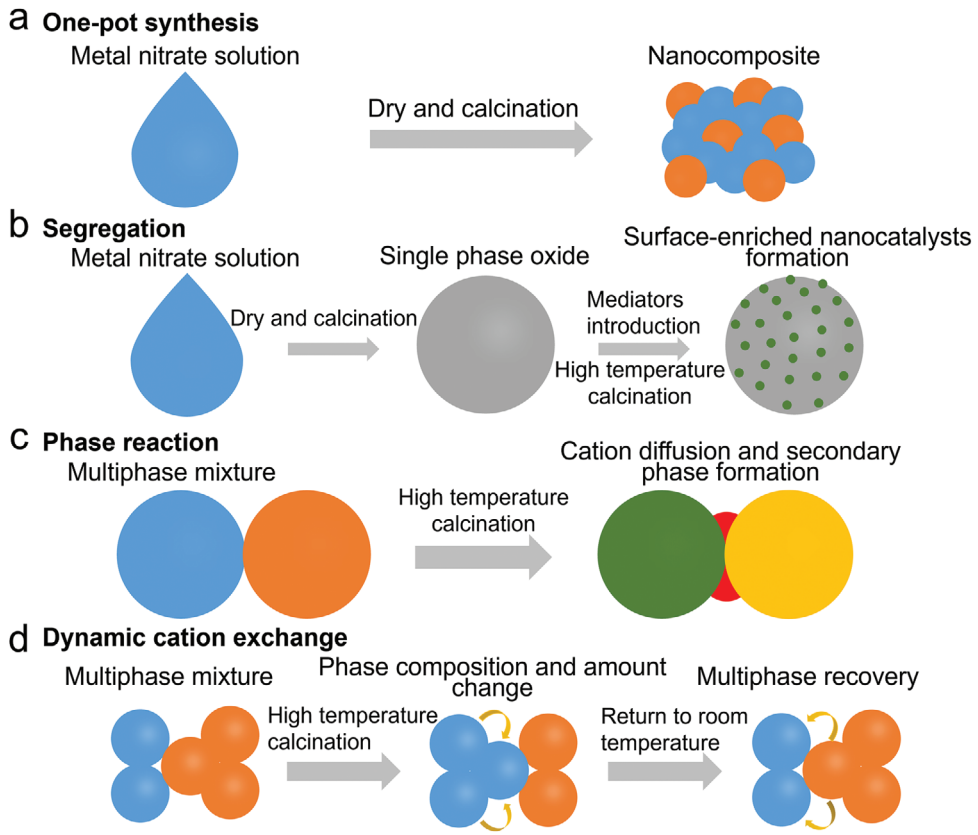

Figure 4. Schematic representation of SOC fuel electrode in situ assembly processes: a) one-pot synthesis leading to nanocomposite formation, b) segregation process resulting in surface-enriched nano-catalysts, c) phase reaction with cation diffusion and secondary phase formation, and d) dynamic cation exchange modifying phase composition.

phases (Figure 4d), ultimately influencing the electrocatalytic activity of the air electrode.[31]

4. Recent Advances

4.1. In situ Assembled Composite Materials for SOC Fuel Electrodes

4.1.1. Metal Exsolution

In situ exsolution is a powerful technique for producing metal nano-catalyst-modified perovskite composites for SOC fuel electrodes.[152,163–165] This approach offers distinct advantages over conventional Ni-based cermets, as well as catalysts fabricated by infiltration or vapor-deposition methods. Exsolved nanoparticles are small and strongly anchored to the perovskite substrate. This significantly increases the active surface area for fuel oxidation and formation reactions. Moreover, the strong anchoring prevents nanoparticle sintering. Studies have shown that in situ exsolution can effectively mitigate carbon deposition when hydrocarbon fuels are used and enhance sulfur poisoning resistance. These aspects are discussed in more detail below.

Notably, metal nano-catalysts like Ru,[166,167] and Pd,[160] Ni,[168] Co,[168,170] Fe,[168,171] Cu,[172] have been successfully developed using exsolution. Shen et al. have developed a Pd nanoparticle-decorated perovskite by treating $LaCo_{0.3}Fe_{0.67}Pd_{0.03}O_{3-\delta}$ at 800 °C in H_2. The exsolved Pd significantly enhanced the activity of the fuel electrode toward H_2 oxidization. When operating with H_2 fuel, the SOC supported by SDC and using $LaCo_{0.3}Fe_{0.67}Pd_{0.03}O_{3-\delta}$ as the fuel electrode displayed a maximum power density of 646 mW cm^{-2} at 750 °C, a value higher than that of a conventional Ni-SDC fuel electrode-based cell (471 mW cm^{-2}).[160] He et al. successfully synthesized $Ba(Zr_{0.1}Ce_{0.7}Y_{0.1}Yb_{0.1})_{0.95}Pd_{0.05}O_{3-\delta}$, which was then used in a Ni-$Ba(Zr_{0.1}Ce_{0.7}Y_{0.1}Yb_{0.1})_{0.95}Pd_{0.05}O_{3-\delta}$ H-SOC fuel electrode cermet. While operating this electrode, Pd nanoparticles exsolved, resulting in improved NH_3 decomposition and enhanced power output. A Ni-$Ba(Zr_{0.1}Ce_{0.7}Y_{0.1}Yb_{0.1})_{0.95}Pd_{0.05}O_{3-\delta}$-supported H-SOC button cell exhibited a maximum power density of 723 mW cm^{-2} at 650 °C with NH_3 as the fuel. This performance surpassed that of conventional Ni-BZCYYb fuel electrode-based cells, which achieved a power density of 450 mW cm^{-2}. Similarly, Song et al. effectively substituted Ni with Pd in a NiO-$Ba(Zr_{0.1}Ce_{0.7}Y_{0.1}Yb_{0.1})_{0.95}Pd_{0.05}O_{3-\delta}$ fuel electrode, leading to improved power output in direct ammonia H-SOC.[142] Park et al. developed a perovskite fuel electrode modified with Co nanoparticles for CO_2 electrolysis by treating $La_{0.6}Sr_{0.4}Co_{0.7}Mn_{0.3}O_{3-\delta}$ at 800 °C under 20 vol% H_2—N_2 atmosphere. Exsolved Co nanoparticles catalyzed the CO_2 reduction reaction, while simultaneously increasing oxygen vacancy concentration to promote CO_2 adsorption, thus enhancing the overall reaction activity.[173]

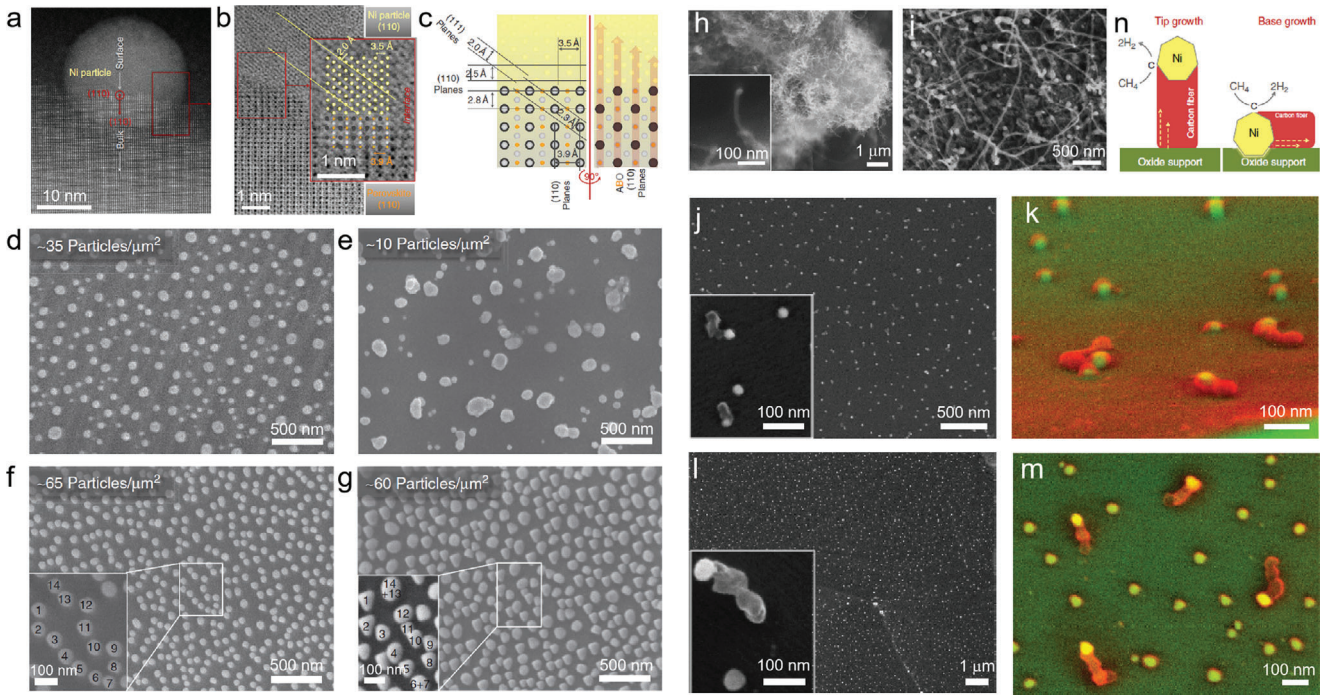

Figure 5. Morphological analysis of Ni nanoparticles and their interaction with a La-Sr-Ti-containing perovskite oxide: a) TEM image of a single Ni nanoparticle exsolved from $La_{0.52}Sr_{0.28}Ti_{0.94}Ni_{0.06}O_{3-\delta}$ under 3 vol% H_2O-5 vol% H_2-92 vol% Ar at 930 °C for 60 h. b) High-resolution TEM images of the Ni/perovskite interface. c) Atomic model illustrating the metal-perovskite interface. SEM images depicting vapor-deposited Ni particles on $La_{0.4}Sr_{0.4}TiO_{3-\delta}$ d) before and e) after H_2 treatment (650 °C, 24 h and 800 °C, 6 h). Ni nanoparticles on $La_{0.52}Sr_{0.28}Ti_{0.94}Ni_{0.06}O_{3-\delta}$ f) before and g) following processing in 5 vol%H_2—Ar atmospheres at 900 °C for 12 h. SEM images showing Ni particles obtained by h) infiltration and i) vapor-deposition on $La_{0.4}Sr_{0.4}TiO_{3-\delta}$ after coking under 20 vol% CH_4/H_2 at 800 °C for 4 h. j) SEM and k) corresponding false-color micrographs of Ni nanoparticles exsolved from $La_{0.52}Sr_{0.28}Ti_{0.94}Ni_{0.06}O_{3-\delta}$ (under 5 vol%H_2—Ar at 880 °C for 6 h) after coking under 20 vol% CH_4/H_2 at 800 °C for 4 h. l) SEM and m) corresponding false-color micrographs of Ni nanoparticles exsolved from $La_{0.52}Sr_{0.28}Ti_{0.94}Ni_{0.06}O_{3-\delta}$ (under 5 vol%H_2—Ar at 1000 °C for 6 h) after coking under 20 vol% CH_4/H_2 at 800 °C for 4 h. n) Coke formation schematic. Reproduced with permission.[23] Copyright 2015, Nature Publishing Group.

Neagu and colleagues demonstrated that the exsolved Ni nano-catalysts tend to sinter far less than vapor-deposited Ni nanoparticles.[23] This remarkable anti-sintering property is likely due to the epitaxial embedding of the metal nanoparticles into the oxide (**Figure 5a–c**). For instance, while vapor-deposited Ni nanoparticles exhibited rapid agglomeration within 6 hours at 800 °C (Figure 5d,e), in situ exsolved Ni nanoparticles demonstrated remarkable stability even after 24 hours at 900 °C (Figure 5f,g).[174] Kyriakou et al. showed that exsolved Ni nanoparticles originating from $La_{0.43}Ca_{0.37}Ti_{0.94}Ni_{0.06}O_{3-\delta}$ were stable in CO_2/H_2O electrolysis at an electrolysis current density of −0.6 A cm^{-2} at 850 °C, with the voltage increasing modestly from 1.37 to 1.39 V. Conversely, a conventional Ni-YSZ fuel electrode-based cell experienced a rapid increase in voltage from 1.54 to 2.03 V over the course of 48 hours. SEM analysis showed that conventional Ni-YSZ electrodes experienced severe Ni coarsening and Ni nanoparticles exsolved from $La_{0.43}Ca_{0.37}Ti_{0.94}Ni_{0.06}O_{3-\delta}$ were almost unchanged while experiencing identical conditions.[175]

In situ exsolution of metal nano-catalysts from oxide substrates offers enhanced resistance to coke deposition, which is generally a major challenge for high-temperature fuel cells. This resistance stems from the strong catalyst-substrate bonding, which prevents separation during carbon fiber growth.[23] Neagu et al. compared exsolved Ni nanoparticles to those deposited by infiltration (Figure 5h) or vapor deposition (Figure 5i). Deposited particles experienced significant fiber growth at the Ni–*p*erovskite interface, causing particle uplift (Figure 5j-m) due to the "tip-growth" mechanism. In contrast, exsolved Ni particles exhibited minimal carbon fiber growth and remained firmly anchored to the substrate (Figure 5n), thereby inhibiting fiber formation.[175]

Exsolution offers a promising approach for developing fuel electrodes with enhanced durability in harsh operating environments. This technique not only mitigates carbon deposition, a common challenge in fuel cells but also modifies the interaction between the metal catalyst and the oxide host. This alteration, in turn, influences the metal's surface electronic structure, leading to reduced sulfur adsorption and improved sulfur tolerance. For example, Song et al. prepared a Ni nanoparticle-decorated $La_{0.35}Ca_{0.50}TiO_{3-\delta}$ perovskite fuel electrode, which was optimized for H_2S-containing fuel, by reducing $La_{0.33}Ca_{0.47}Ti_{0.94}Ni_{0.06}O_{3-\delta}$ at 800 °C under H_2. Compared to conventional Ni catalysts in Ni-SDC fuel electrodes, the anchoring state may change the electronic structure of each individual phase of the composite, suppressing sulfur adsorption and increasing operational stability in H_2S-containing fuel.[92]

In a groundbreaking study, O'Hayre et al. developed a nano Ni catalyst modified Ni-$BaZr_{0.8}Y_{0.2}O_{3-\delta}$ fuel electrode through

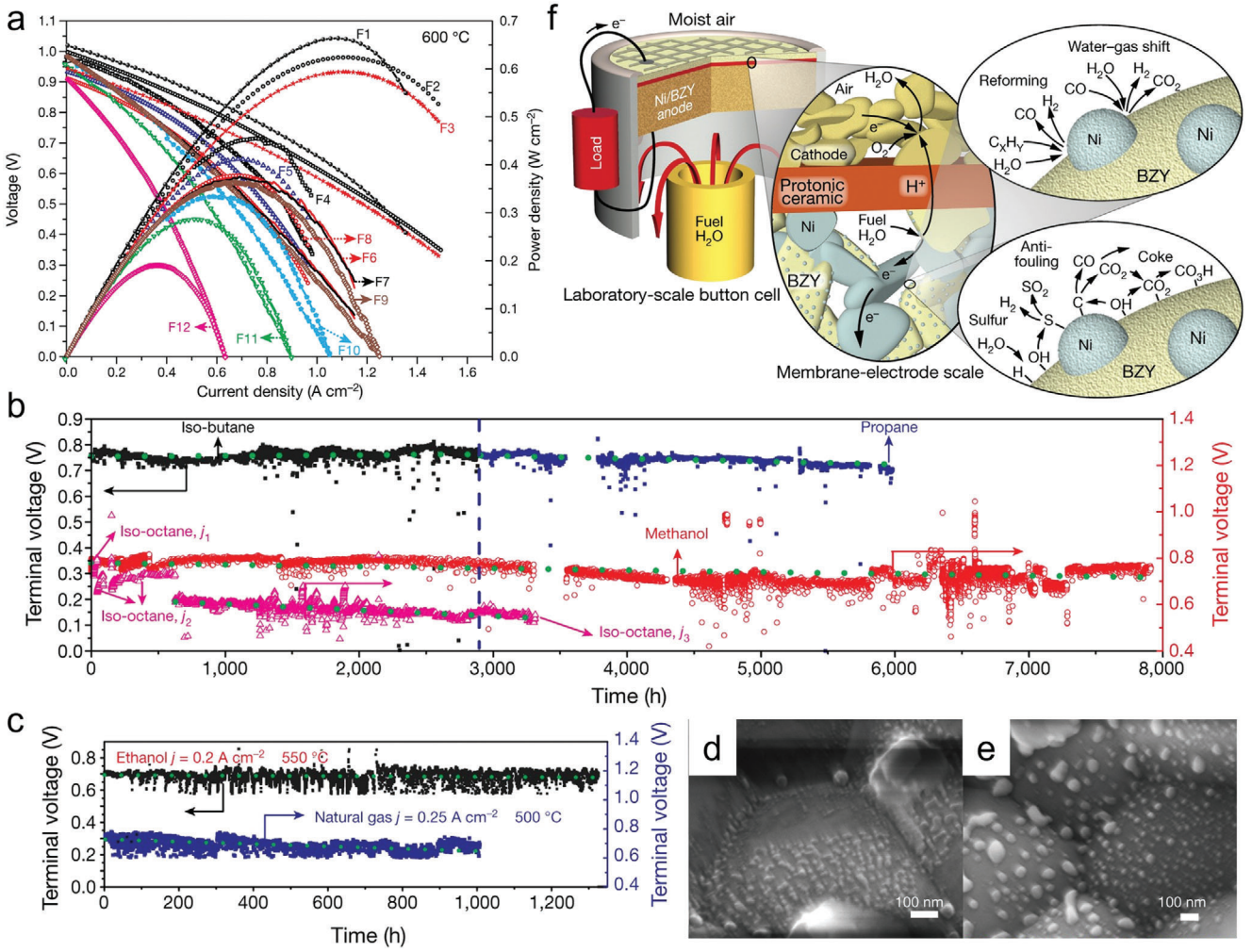

Figure 6. Electrochemical performance and stability of H-SOCs with the Ni-$BaZr_{0.8}Y_{0.2}O_{3-\delta}$ anode. a) Current-voltage (*I–V*) and power density (*I–P*) characteristics at 600 °C for various fuels including H_2 (F1), NH_3 (F2), CH_3OH (F3), iso-C_4H_{10} (F4), n-C_4H_{10} (F5), natural gas (F6), 19.5 ppm H_2S-contaminated natural gas (F7), C_3H_8 (F8), CH_4 (steam/carbon ratio = 2, F9), C_2H_5OH (F10), CH_4 (steam/carbon ratio = 2.5, F11), and iso-C_8H_{18} (F12). b) Long-term operational stability with iso-C_4H_{10}, C_3H_8, iso-C_8H_{18}, and CH_3OH; c) C_2H_5OH and natural gas. SEM images of Ni-doped $BaZr_{0.8}Y_{0.2}O_{3-\delta}$ electrode after stability testing in humidified CH_4 for d) 300 hours and e) 1400 hours at 500 °C. f) Schematic overview of H-SOC functionality: hydrocarbon reforming, water-gas shift reactions, and sulfur and coke mitigation mechanisms. Reproduced with permission.[176] Copyright 2018, Macmillan Publishers Ltd., part of Springer Nature.

the in situ exsolution method, which dramatically enhanced the performance of conventional Ni-based H-SOC fuel electrodes. This novel fuel electrode composition exhibited exceptional activity, coking resistance, sulfur tolerance, and anti-sintering properties. Using solid-state reactive sintering, the authors fabricated a fuel-electrode-supported H-SOC. The small amount of Ni incorporated into the $BaZr_{0.8}Y_{0.2}O_{3-\delta}$ during powder preparation subsequently exsolved during operation. This H-SOC demonstrated PPDs ranging from 0.66 W cm^{-2} for H_2 to 0.17 W cm^{-2} for iso-octane in 11 different fuels (**Figure 6a**). The cells maintained similar PPDs when exposed to natural gas with and without H_2S impurity (19.5 ppm), showcasing sulfur tolerance.

Impressively, long-term stability tests over several thousand hours with various hydrocarbon fuels confirmed its outstanding coking resistance (Figure 6b,c). Interestingly, the exsolved Ni nanoparticles displayed minimal size increase during operation, indicating excellent resistance to sintering (Figure 6d,e). The enhanced coke resistance and sulfur tolerance were attributed to the nano-socketed Ni nano-catalysts and the strong water storage capability of $BaZr_{0.8}Y_{0.2}O_{3-\delta}$ perovskite. The exsolved Ni particles, which were firmly anchored to the substrate (Figure 5n), inhibited carbon fiber formation by preventing Ni lift-off. Additionally, $BaZr_{0.8}Y_{0.2}O_{3-\delta}$ effectively removed adsorbed sulfur from H_2S impurity and deposited coke by utilizing its stored water (Figure 6f).[18]

4.1.2. Alloy Exsolution

Alloy exsolution in perovskites containing at least two easily reducible transition metal cations, such as Ni,[24,116,154,177–180]

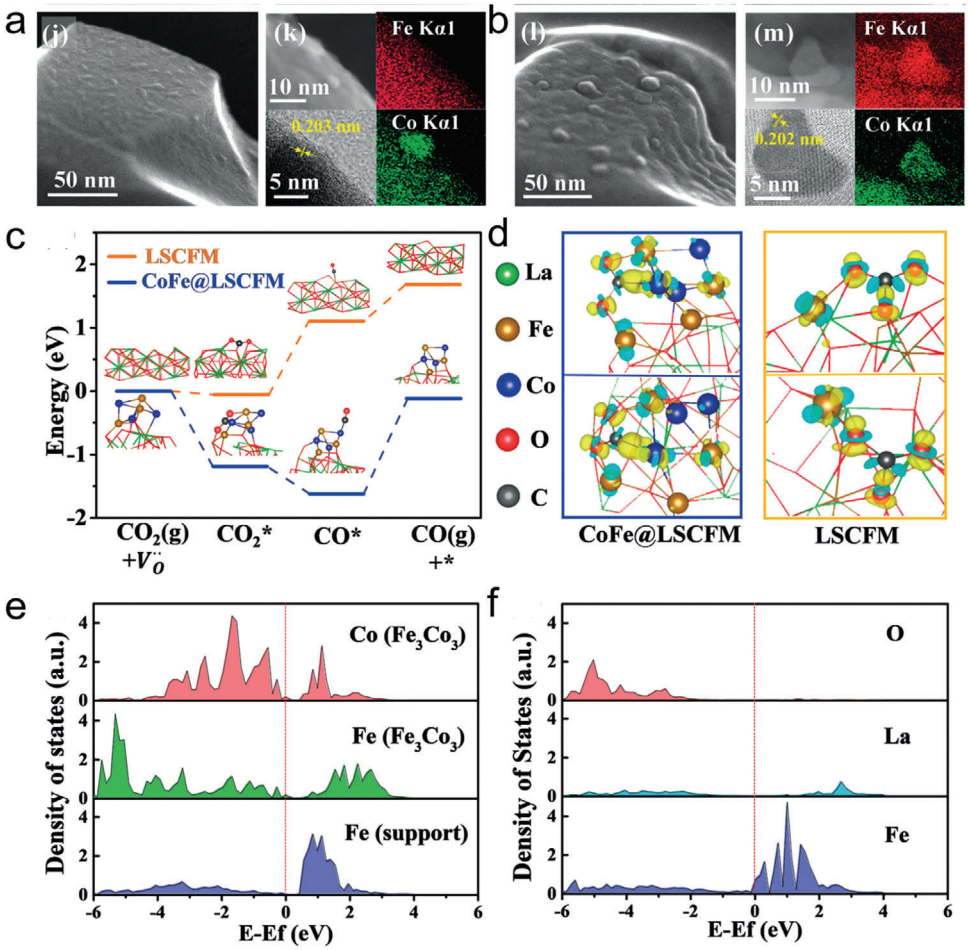

Figure 7. In situ STEM images and corresponding cation mapping of LSCFM reduction at a) 600 °C and b) 700 °C in 10 Pa H_2. Density functional theory calculation results. c) Energy diagram of CO_2 electrolysis over the LSCFM surface and the CoFe@LSCFM interface. $V_o^{\cdot\cdot}$ denotes an oxygen vacancy, CO_2* and CO* are intermediates. d) Charge density differences isosurface of CO_2* on the CoFe@LSCFM interface and LSCFM surface. The DOS of active centers of CO_2 adsorption before adsorption: e) CoFe@LSCFM interface and f) LSCFM surface. Reproduced with permission.[189] Copyright 2020, Wiley-VCH Verlag GmbH & Co. KGaA, Weinheim.

Co,[165,181–185] and Fe,[24,116,154,178–188] is an in situ assembly process taking place at high temperatures and in a reducing environment. These cations migrate to the surface at these conditions, are reduced into metallic form, nucleate, and form nanoparticles. Exsolved alloy nano-catalysts, like their metallic components, are characterized by high specific surface area and strong anchoring to the perovskite support but also benefit from enhanced electrocatalytic activity due to synergistic interactions among the two metal components and the oxide substrate. Furthermore, these catalysts often demonstrate improved resistance to sulfur poisoning and coke formation.

Wang et al. investigated alloy exsolution in $La_{0.4}Sr_{0.6}Co_{0.2}Fe_{0.7}Mo_{0.1}O_{3-\delta}$ (LSCFM) using operando high-resolution transmission electron microscopy. Under 10 Pa H_2 at 600 °C, initial exsolution of Co was observed due to its higher reducibility (**Figure** 7a). When the temperature increased to 700 °C, Fe also exsolved, resulting in the formation of CoFe alloy nanoparticles (Figure 7b). Density functional theory calculations corroborated these findings, demonstrating a lower segregation energy for Co compared to Fe.[189]

Combining the alloy with the LSCFM substrate has improved CO_2 electrolysis. Experiments showed a 21% increase in current density for the CoFe@LSCFM cell compared to the LSCFM control (1.45 A cm^{-2} vs 1.20 A cm^{-2}). This suggests that adding the CoFe nanoalloy makes the electrolysis process more efficient. Density functional theory analysis indicates the CoFe cluster binds CO_2 and improves CO_2 adsorption over the metal-oxide interface (Figure 7c,d). Further analysis of the partial density of states (DOS) suggests that CoFe@LSCFM is more active than LSCFM in adsorbing and activating CO_2 (Figure 7e,f).[189] Other studies support using alloy nano-catalysts with perovskite materials to improve CO_2 electrolysis. Examples include $CoFe@La_{0.4}Sr_{0.6}Co_{0.2}Fe_{0.7}Nb_{0.1}O_{3-\delta}$,[190] $FeNi_3@Sr_2Fe_{1.35}Mo_{0.45}Ni_{0.2}O_{6-\delta}$,[179] $FeNi_3@La_{0.6}Sr_{0.4}Fe_{0.8}Ni_{0.2}O_{3-\delta}$,[191] $NiFe@Sr_{1.9}Fe_{1.5}Mo_{0.4}Ni_{0.1}O_{6-\delta}$,[192] and $Co_3Fe_7@Sr_2Ti_{0.8}Co_{0.2}FeO_6$.[193] These systems consistently demonstrate enhanced CO_2 electrolysis performance, emphasizing the

significant potential of nano-alloy catalysts in CO_2 conversion technologies.

Wang et al. recently advanced the development of high-density nano-CoFe alloy-modified perovskite fuel electrodes for efficient partial methane reforming O-SOC. By controlling Co substitution in $La_{0.6}Sr_{0.4}Ti_{0.3}Fe_{0.7}O_{3-\delta}$ perovskite, they effectively lowered the average B-site metal exsolution energy, facilitating the formation of the active nano-CoFe alloy. The optimized $La_{0.6}Sr_{0.4}Ti_{0.3}Fe_{0.5}Co_{0.2}O_{3-\delta}$ fuel electrode demonstrated exceptional performance in partial methane reforming, achieving a CH_4 conversion of 86.9% and CO selectivity of 90.1% at 800 °C. Remarkably, the O-SOC exhibited stable operation exceeding 1250 hours, maintaining a CO selectivity above 95%.[194]

Duan et al. synthesized a $Sm_{0.2}Ce_{0.7}Ni_{0.1}Ru_{0.05}O_{2-\delta}$ (SCNR) catalyst via co-doping CeO_2 with Sm, Ni, and Ru. Subsequently, they treated the SCNR with 20 vol% H_2—Ar for 30 min at 600 °C to acquire a SCNR-supported Ni-Ru bimetallic catalyst. Catalytic testing revealed that the Ni-Ru modified SCNR catalyst exhibited a methane partial reforming conversion of 33.9% at 650 °C, significantly outperforming the $Sm_{0.2}Ce_{0.7}Ni_{0.15}O_{2-\delta}$ (27.1%), $Sm_{0.2}Ce_{0.7}Ru_{0.15}O_{2-\delta}$ (18.3%), and $Ce_{0.9}Ni_{0.1}Ru_{0.05}O_{2-\delta}$ (23.5%) catalysts. Density functional theory calculations revealed that the synergistic interaction between Ni and Ru sites lowers the activation energy for the initial C-H bond cleavage, promoting CH_x decomposition. Furthermore, Sm doping enhances the concentration of oxygen vacancies in CeO_2, facilitating H_2O adsorption and dissociation. Consequently, the Ni-Ru modified SCNR catalyst exhibits the capability for concurrent activation of both CH_4 and H_2O molecules while oxidizing the CH* intermediates and demonstrating improved coking tolerance. When employing the Ni—Ru modified SCNR as the fuel electrode catalyst layer in an O-SOC device, the cell exhibited a peak power density of 733 mW cm^{-2} at 650 °C using humidified methane as fuel (O/C = 1/2), significantly outperforming the uncoated O-SOC (473 mW cm^{-2}).[195]

Alloy exsolution can lead to the formation of multiple-twinned alloy nanoparticles. This happens because Co and Fe diffuse at different speeds, causing the crystals to grow in mismatched directions. These complex structural irregularities significantly change the catalyst's electronic and electrocatalytic properties, ultimately boosting its performance. Research by Liu et al. investigated the exsolution of Co and Fe in $Sr_2CoMo_{0.95}Fe_{0.05}O_{6-\delta}$. They observed multiple-twinned defects on the CoFe alloy surface, which correlated with high activity in both H_2 and CH_4 oxidation reactions. An O-SOC utilizing LSGM support and a $Sr_2CoMo_{0.95}Fe_{0.05}O_{6-\delta}$ fuel electrode achieved a PPD of 993 mW cm^{-2} with hydrogen fuel and 652 mW cm^{-2} with methane fuel at an operating temperature of 850 °C.[196] Beyond electrochemical activity, the interaction between the individual metals within the exsolved alloy can also improve coke tolerance. A variety of in situ exsolved alloy nano-catalysts decorated perovskites, such as $CoFe@Sr_2FeMo_{2/3}Co_{1/3}O_{6-\delta}$, $CoFe@Pr_{0.4}Sr_{0.6}Co_{0.2}Fe_{0.7}Mo_{0.1}O_{3-\delta}$,[165] $FeNi@La_{0.7}Sr_{0.3}Cr_{0.85}Fe_{0.03}Ni_{0.12}O_{3-\delta}$,[197] $FeNi@La_{0.5}Sr_{0.5}Fe_{0.8}Ni_{0.2}O_{3-\delta}$,[188] $CoFe@Sr_2Co_{0.4}Fe_{1.2}Mo_{0.4}O_{6-\delta}$,[196] and $FeNi_3@Sr_2FeMo_{0.65}Ni_{0.35}O_{6-\delta}$,[154] were successfully developed achieving excellent coke tolerance in hydrocarbon fuels (i.e., CH_4, C_2H_6, and C_3H_8).

The interaction between metals within the exsolved alloy can improve the catalyst's ability to adsorb fuel, enhance its catalytic activity, and make it more resistant to impurities. Barnett et al. developed the in situ exsolved, FeRu-decorated material $SrTi_{0.3}Fe_{0.7}Ru_{0.07}O_{3-\delta}$, which suggested enhanced H_2 adsorption capability relative to $SrTi_{0.3}Fe_{0.7}O_{3-\delta}$ perovskite as the FeRu alloy nanoparticle accelerated H_2 dissociation, which is a rate-limiting step for H_2 oxidization reaction. In a study utilizing an LSGM-supported button cell, the fuel electrode material $SrTi_{0.3}Fe_{0.7}Ru_{0.07}O_{3-\delta}$ demonstrated a PPD of 0.68 W cm^{-2} at 800 °C when operating under a H_2 fuel with 3 vol% of steam. This PPD was slightly lower compared to the cell employing $SrTi_{0.3}Fe_{0.7}O_{3-\delta}$ as the fuel electrode, which achieved a PPD of 0.74 W cm^{-2} under identical conditions. However, interestingly, when the cell temperature was maintained at 800 °C and the fuel composition was switched from 97 vol% H_2-3 vol% H_2O to 29.1 vol% H_2-3 vol% H_2O, the cell featuring $SrTi_{0.3}Fe_{0.7}Ru_{0.07}O_{3-\delta}$ as the fuel electrode exhibited a higher PPD of 0.54 W cm^{-2} compared to the analogous cell with $SrTi_{0.3}Fe_{0.7}O_{3-\delta}$ as the fuel electrode, which achieved a PPD of 0.34 W cm^{-2}. These results provided confirmation of the enhanced H_2 adsorption capabilities of the nano FeRu alloy catalyst, contributing to its improved performance.[178]

Shao et al. developed in situ exsolved NiCo alloy nano-catalysts on a $La_{0.50}Sr_{0.30}TiO_{3-\delta}$ perovskite substrate by treating a $La_{0.52}Sr_{0.28}Ti_{0.94}Ni_{0.03}Co_{0.03}O_{3-\delta}$ powder at 800 °C under H_2. The interaction between exsolved Ni and Co resulted in optimized NH_3 adsorption and N_2 desorption characteristics, promoting NH_3 decomposition. Consequently, SOCs incorporating reduced $La_{0.52}Sr_{0.28}Ti_{0.94}Ni_{0.03}Co_{0.03}O_{3-\delta}$ demonstrated superior performance as direct-ammonia fuel electrodes (NH_3 fuel, 800 °C, PPD of 361 mW cm^{-2}) relative to cells using $La_{0.52}Sr_{0.28}Ti_{0.94}Ni_{0.06}O_{3-\delta}$ (PPD of 161 mW cm^{-2}) and $La_{0.52}Sr_{0.28}Ti_{0.94}Co_{0.06}O_{3-\delta}$ (PPD of 98 mW cm^{-2}) as fuel electrodes.[22] Studies demonstrate the superior sulfur tolerance of in situ exsolved alloy catalysts. Luo et al. developed in situ exsolved FeNi alloy nano-catalysts embedded in $La_{0.7}Sr_{0.3}CrO_{3-\delta}$. This electrode exhibited remarkable resistance to sulfur poisoning when an H_2S-containing fuel was used. A YSZ-supported SOC incorporating the Ni-Fe-decorated $La_{0.7}Sr_{0.3}CrO_{3-\delta}$ as the fuel electrode achieved a PPD of 560 mW cm^{-2} when operated with 5000 ppm H_2S-H_2 fuel at 800 °C. This PPD significantly exceeded the performance of fuel electrodes decorated with either Ni (460 mW cm^{-2}) or Fe (360 mW cm^{-2}) nano-catalysts on $LaSrCrO_{3-\delta}$.[197]

4.1.3. Oxide Segregation

Fuel electrode materials in SOCs frequently exhibit oxide segregation during operation. This segregation arises from two primary mechanisms. First, the exsolution of B-site cations destabilizes the perovskite structure by removing BO_6 octahedra. Consequently, A-site metal oxides segregate to the surface.[26] Under SOC conditions, perovskites can transition from disordered-type to A-site-ordered-type, inducing B-site metal oxide segregation. Importantly, in situ, segregated oxides influence the activity and durability of fuel electrodes in both fuel cell and electrolysis operations.

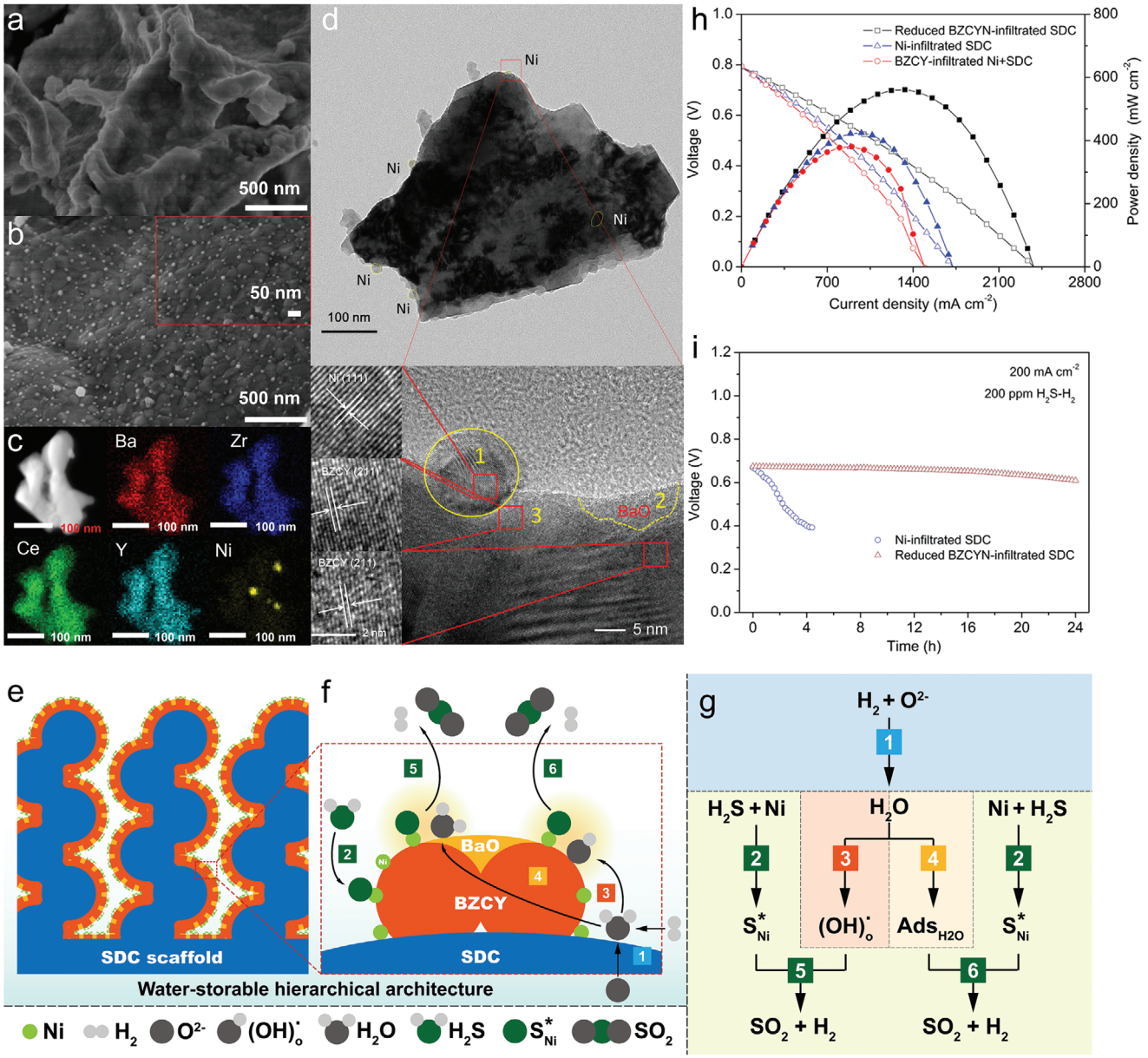

Figure 8. Scanning electron microscopy (SEM) images of BZCYN a) before and b) after H_2 treatment at 800 °C, showcasing surface modifications. c) STEM-EDX mapping of reduced BZCYN demonstrates elemental distribution. d) High-resolution transmission electron microscopy (TEM) images of reduced BZCYN highlight the interface between Ni particles and the BZCYN matrix. e) Schematic illustrations depict the hierarchical water-stable fuel electrode structure and f,g) the detailed sulfur removal mechanism with key steps labeled. h) Current-voltage (*I–V*) and power density (*I–P*) curves for SDC-supported cells with various fuel electrodes: BZCYN-infiltrated SDC, Ni-infiltrated SDC, and $BaZr_{0.4}Ce_{0.4}Y_{0.2}O_{3-\delta}$ (BZCY)-infiltrated Ni-SDC. All cells were tested at 800 °C using 200 ppm H_2S-H_2 fuel. i) Comparative stability test for cells with BZCYN-infiltrated SDC and Ni-infiltrated SDC electrodes under 200 ppm H_2S-H_2 fuel at 800 °C. Reproduced with permission.[26] Copyright 2017, WILEY-VCH Verlag GmbH & Co. KGaA, Weinheim.

Shao et al. developed $Ba(Zr_{0.4}Ce_{0.4}Y_{0.2})_{0.8}Ni_{0.2}O_{3-\delta}$ (BZCYN) to enhance sulfur tolerance in fuel electrodes. Under O-SOC fuel electrode conditions, Ni exsolution from the BZCYN lattice promoted the segregation of amorphous BaO from the A-site (**Figure** 8a–d). In H_2S-containing fuels, segregated BaO demonstrated strong H_2O adsorption (Figure 8e,f). This adsorbed water reacted with adsorbed sulfur on the Ni catalyst surface, forming SO_2 and H_2 (Figure 8g), thus improving sulfur tolerance compared to conventional Ni-SDC fuel electrodes. An SDC-supported button cell featuring reduced BZCYN-infiltrated SDC as the fuel electrode achieved a maximum power density of 561 mW cm^{-2} (800 °C, 200 ppm H_2S-H_2 fuel). This performance significantly exceeded cells using Ni-infiltrated SDC and BZCY-infiltrated Ni-SDC fuel electrodes (Figure 8h). Moreover, the BZCYN-infiltrated SDC fuel electrode demonstrated superior operational stability over the Ni-infiltrated SDC fuel electrode in 200 ppm H_2S-H_2 fuel (Figure 8i).[26] Similar improvements were observed by Guo et al. with a

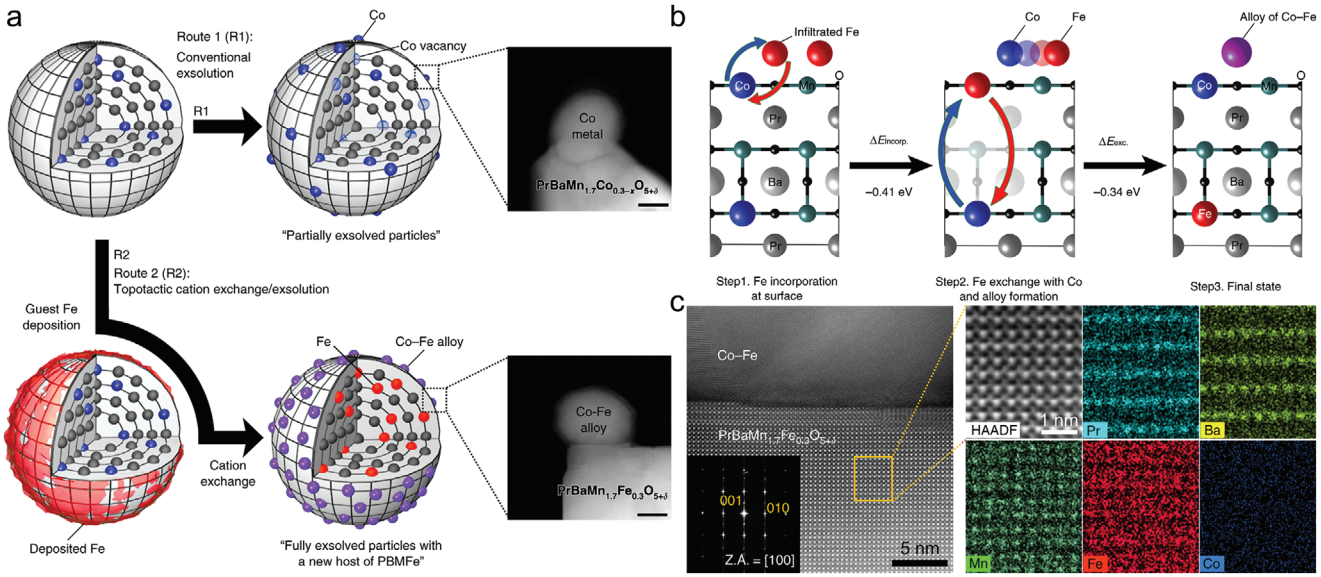

Figure 9. Comparison of exsolution processes, energetics, and structural analysis of $PrBaMn_{1.7}Co_{0.3}O_{5+\delta}$-Fe with topotactic exsolution. a) Schematic illustrating the difference between conventional and topotactic exsolution. b) Topotactic cation exchange energetics between Fe cations (in oxide) and Co cations in the $PrBaMn_{1.7}Co_{0.3}O_{5+\delta}$ host. c) High-resolution TEM image of $PrBaMn_{1.7}Co_{0.3}O_{5+\delta}$-Fe after topotactic exsolution, with an inset showing the corresponding fast Fourier transform image and atom map. Reproduced with permission.[25] Copyright 2019, Nature Publishing Group.

$Ba_{0.3}Sr_{0.7}Fe_{0.9}Mn_{0.1}O_{3-\delta}$ catalyst in CH_4 fuel. During SOC operation, Fe exsolution triggered A-site SrO segregation. SrO's water adsorption properties played a crucial role in coke removal, thus enhancing coke tolerance. This resulted in stable SOC operation with a reduced $Ba_{0.3}Sr_{0.7}Fe_{0.9}Mn_{0.1}O_{3-\delta}$ fuel electrode in CH_4 fuel.[164] Ni et al. further demonstrated this concept with $Sr_{0.8}Ce_{0.2}Fe_{0.95}Ru_{0.05}O_{3-\delta}$ for C_3H_8 fuel. Here, A-site SrO and CeO_2 segregation occurred alongside B-site Ru exsolution. Exsolved Ru enhanced H_2 oxidation, while segregated CeO_2 improved C_3H_8 adsorption, and SrO boosted coke resistance due to its superior water adsorption ability.[198]

In fuel cell mode, segregated oxides promote better fuel and water adsorption, improving fuel oxidation activity and tolerance to impurities. For instance, BZCYN and $Ba_{0.3}Sr_{0.7}Fe_{0.9}Mn_{0.1}O_{3-\delta}$ have been developed as catalysts for enhancing the sulfur tolerance of fuel electrodes by driving the segregation of BaO and SrO, respectively. Similarly, in electrolysis mode, oxide segregation can promote the adsorption of the reactants, enhancing electrolysis performance. $La_{0.6}Ca_{0.4}Fe_{0.8}Ni_{0.2}O_{3-\delta}$ and $La_{0.4}Sr_{0.55}Co_{0.2}Fe_{0.6}Nb_{0.2}O_{3-\delta}$ have been proposed as fuel electrode catalysts for CO_2 and H_2O electrolysis, respectively, with their in situ exsolved oxides improving CO_2 and H_2O adsorption, promoting electrolysis activity.[180] Yang et al. proposed $La_{0.4}Sr_{0.55}Co_{0.2}Fe_{0.6}Nb_{0.2}O_{3-\delta}$ as a fuel electrode for H_2O electrolysis. Under H_2 at 800 °C, a Co_2Fe alloy exsolved in situ concomitantly with SrO segregation. Due to this joint process, Co_2Fe and SrO formed an intimate interface. The in situ exsolved SrO exhibited strong water adsorption capability, accelerating the water adsorption process and consequently delivering superior water electrolysis performance.[184]

Kim et al. observed the formation of MnO nano-catalysts during the phase transition from disordered $Nd_{0.5}Ba_{0.5}MnO_{3-\delta}$ to A-site ordered $NdBaMn_2O_{5+\delta}$ under high-temperature reducing conditions. These MnO nanoparticles exhibited excellent electrocatalytic activity toward fuel oxidation.[156] Similarly, Yu et al. developed $Pr_{0.9}Ba_{0.9}Mn_{0.82}Fe_{0.18}O_{5+\delta}$ as a fuel electrode catalyst for CO_2 electrolysis by introducing A-site deficiency and B-site Fe substitution. Under high-temperature conditions, the phase transition and A-site deficiency facilitated the exsolution of Fe and segregation of MnO, enhancing CO_2 adsorption and consequently improving CO_2 electrolysis performance.[199]

4.1.4. Topotactic Exsolution

Conventional exsolution methods used in fuel electrodes can lead to phase transitions or decomposition, undermining electrode stability. To overcome these limitations, the topotactic exsolution approach has emerged. This strategy leverages topotactic cationic exchange as internal cations migrate to the surface while externally introduced cations fill the vacated sites. Topotactic exsolution enables the formation of metal nano-catalysts in situ. This happens without forming (potentially destabilizing) cation deficiencies normally found in conventional exsolution. By avoiding detrimental phase transitions and decomposition associated with traditional exsolution techniques, topotactic exsolution offers a promising pathway toward more robust and efficient fuel electrodes.

Kim et al. demonstrated the enhancement of perovskite catalysts via topotactic exsolution. By introducing Fe guest cations, they successfully displaced Co cations within the $PrBaMn_{1.7}Co_{0.3}O_{5+\delta}$ bulk. This process significantly increased exsolved nanoparticles, enhancing catalytic activity (**Figure 9a**). Ab initio simulations confirmed the thermodynamic feasibility of the cation exchange process. Initially, deposited Fe was incorporated into the near-surface region of $PrBaMn_{1.7}Co_{0.3}O_{5+\delta}$ by exchanging its position with Co or Mn. The significantly

lower exchange energy of Fe↔Co (−0.41 eV) relative to Fe↔Mn (0.22 eV) indicates a preference for Fe to exchange with Co. Following Fe incorporation, its subsequent exchange with bulk Co is thermodynamically favorable with an exchange energy of −0.34 eV (Figure 9b). This suggests that Fe incorporation actively promotes the exsolution of Co. Direct atom mapping confirmed the Co/Fe exchange (Figure 9c). With more exsolved catalytic nanoparticles, the modified $PrBaMn_{1.7}Co_{0.3}O_{5+\delta}$-Fe exhibited enhanced catalytic performance toward hydrogen oxidation and methane/carbon dioxide reforming reactions. A button cell using LSGM support with $PrBaMn_{1.7}Co_{0.3}O_{5+\delta}$-Fe as the fuel electrode reached a power density of 1.834 W cm^{-2} at 800 °C, a significant improvement over the 0.962 W cm^{-2} achieved by $PrBaMn_{1.7}Co_{0.3}O_{5+\delta}$. In methane/carbon dioxide reforming, the modified perovskite achieved a CO_2 conversion rate of 30%, nearly doubling the performance of the unmodified material.[25]

Luo et al. demonstrated the potential of topotactic exsolution to enhance the stability of perovskite electrodes in O-SOC for CO_2 reduction. By incorporating Fe cations into the $Sr_2Fe_{1.3}Ni_{0.2}Mo_{0.5}O_{6-\delta}$ perovskite lattice, they induced the displacement of Ni cations, leading to an increased density of exsolved metal nanoparticles on the surface. Critically, the introduced Fe cations concurrently replenished B-site vacancies generated by Ni exsolution, effectively stabilizing the perovskite bulk structure. When employed as a fuel electrode in a YSZ-supported O-SOC, the Fe-modified $Sr_2Fe_{1.3}Ni_{0.2}Mo_{0.5}O_{6-\delta}$ exhibited more stable electrolysis current density and Faradaic efficiency for CO production during CO_2 reduction. This enhanced stability is attributed to the Fe supplementation, which mitigates nanoparticle sintering and preserves the structural integrity of the exsolved metal nanoparticles.[200]

4.2. In situ Assembled Composite Materials for SOC Air Electrodes

4.2.1. One-Pot Synthesis

High-temperature calcination is a common method for synthesizing single-phase perovskites from precursor materials. However, precise temperature control is crucial. Deviation from the optimal calcination temperature can lead to the formation of undesired secondary oxide phases instead of the targeted single-phase perovskite. When the calcination temperature falls below the threshold required for single-phase formation, secondary oxide, and perovskite phases emerge, introducing functional oxide and perovskite phases that can enhance electrochemical activity. For example, $PrBaCo_2O_{5+\delta}$ (PBC) must be calcined above 1000 °C to form a single phase. Shao et al. explored lower calcination temperatures to 900 °C, starting from the precursors and resulting in a mixture of phases, including PBC, Pr_6O_{11}, $PrCoO_3$ (PCO), and $BaCoO_3$ (BCO). This composite exhibited enhanced ORR activity compared to single-phase PBC. A symmetric cell with an SDC support and the PBC-based composite electrode showed area-specific resistance (ASR) values of 0.068 Ω cm^2 at 600 °C in air, lower than that for single-phase PBC, which was 0.104 Ω cm^2. An O-SOC with a Ni-YSZ fuel electrode and the composite air electrode achieved PPDs of 1.60 W cm^{-2} at 600 °C and 0.53 W cm^{-2} at 500 °C, using H_2 fuel.[201]

In a subsequent study, Liu et al. introduced $PrBa_{0.8}Ca_{0.2}Co_2O_{5+\delta}$ (PBCC) into a porous $La_{0.6}Sr_{0.4}Co_{0.2}Fe_{0.8}O_{3-\delta}$ (LSCF) scaffold. The corresponding electrode was prepared by infiltrating the nitrate PBCC followed by LSCF calcination at 800 °C. The resulting PBCC layer was uniformly coated on the LSCF surface with PCO and BCO nanoparticles enriching the PBCC layer, as depicted in **Figure 10**a,b. By using this electrode in an SDC-supported symmetric cell, these researchers lowered the ASR and corresponding activation energies relative to the bare LSCF, indicating an improved ORR activity (Figure 10c). When the same electrode was used in a Ni-SDC fuel electrode-supported O-SOC, a maximum power density of 1.21 W cm^{-2} was achieved at 600 °C in 3 vol% H_2O-H_2, outperforming the cell with a bare LSCF (0.76 W cm^{-2}) (Figure 10d). The authors employed density functional theory calculations to elucidate the role each phase plays in catalysis within this composite. Their analysis suggests initial O_2 dissociation at oxygen-deficient sites within the BCO phase. Next, the dissociated oxygen atom enters an oxygen vacancy in PBCC, overcoming a 0.72 eV barrier (Figure 10e). Finally, the adsorbed atomic oxygen migrates through the PBCC bulk and enters an oxygen vacancy of LSCF, overcoming a 2.05 eV barrier (Figure 10e). This mechanism reveals a synergistic enhancement of ORR activity within coated LSCF (Figure 10f). In fact, these authors suggest the BCO and PCO nanoparticles increase active sites for O_2 adsorption and dissociation, while the PBCC promotes the transport of dissociated oxygen to LSCF.[202]

Similarly, Shao et al. developed a BCO nano catalyst modified $BaGdCo_2O_{5+\delta}$ composite material ($Ba_{1.1}Gd_{0.9}Co_2O_{5+\delta}$) by altering the stoichiometry of Ba and Gd in the conventional single-phase double perovskite $BaGdCo_2O_{5+\delta}$. The double perovskite phase exhibits superior functionality for both oxygen adsorption and its initial hydrogenation in ORR. Additionally, it serves as a proficient mass transfer conductor for protons and oxygen ions. In contrast, the BCO phase primarily functions as the active reaction site for the final product (H_2O) formation and desorption. This synergistic interaction between the two components underpins the outstanding performance of the material. Consequently, when employed as an air electrode in H-SOC devices fueled by H_2, the cell achieves peak power densities of 1.15 and 0.87 W cm^{-2} at 700 and 650 °C, respectively.[203]

As mentioned above, enhancing the capability of the electrocatalyst to absorb and dissociate oxygen is crucial for improving ORR activity. These properties can be improved by introducing nanoparticles (e.g., BCO and PCO) onto the surface. Shao et al. developed the multi–*p*hase, cobalt-free, perovskite composite $Sr_{0.9}Ce_{0.1}Fe_{0.8}Ni_{0.2}O_{3-\delta}$ (SCFN), using a one-pot sol-gel synthesis method, which enabled in situ nanoparticle assembly.

After calcination of SCFN's precursors at 850 °C, this material included tetragonal $Sr_xCe_yFe_mNi_nO_{3-\delta}$ (T-SCFN) perovskite ($SrFeO_{3-\delta}$ (SF)-type), Ruddlesden-Popper $Sr_4Fe_3O_{10-\delta}$ (RP-SF)-typed $Sr_xCe_yFe_mNi_nO_{3-\delta}$ (RP-SCFN) perovskite, and surface-enriched NiO and CeO_2 nanoparticles.[27] As shown in **Figure 11**, the SF-based phase exhibited a slow oxygen surface exchange (O_2 adsorption/dissociation) rate and O^{2-} bulk diffusion (Figure 11a). The presence of RP-SF-based phase enhanced O^{2-} bulk conductivity (Figure 11b). Surface-enriched NiO and CeO_2 nanoparticles enlarged the reaction regions for O_2 adsorption/dissociation and promoted O^{2-} conduction from the surface to the SF-based

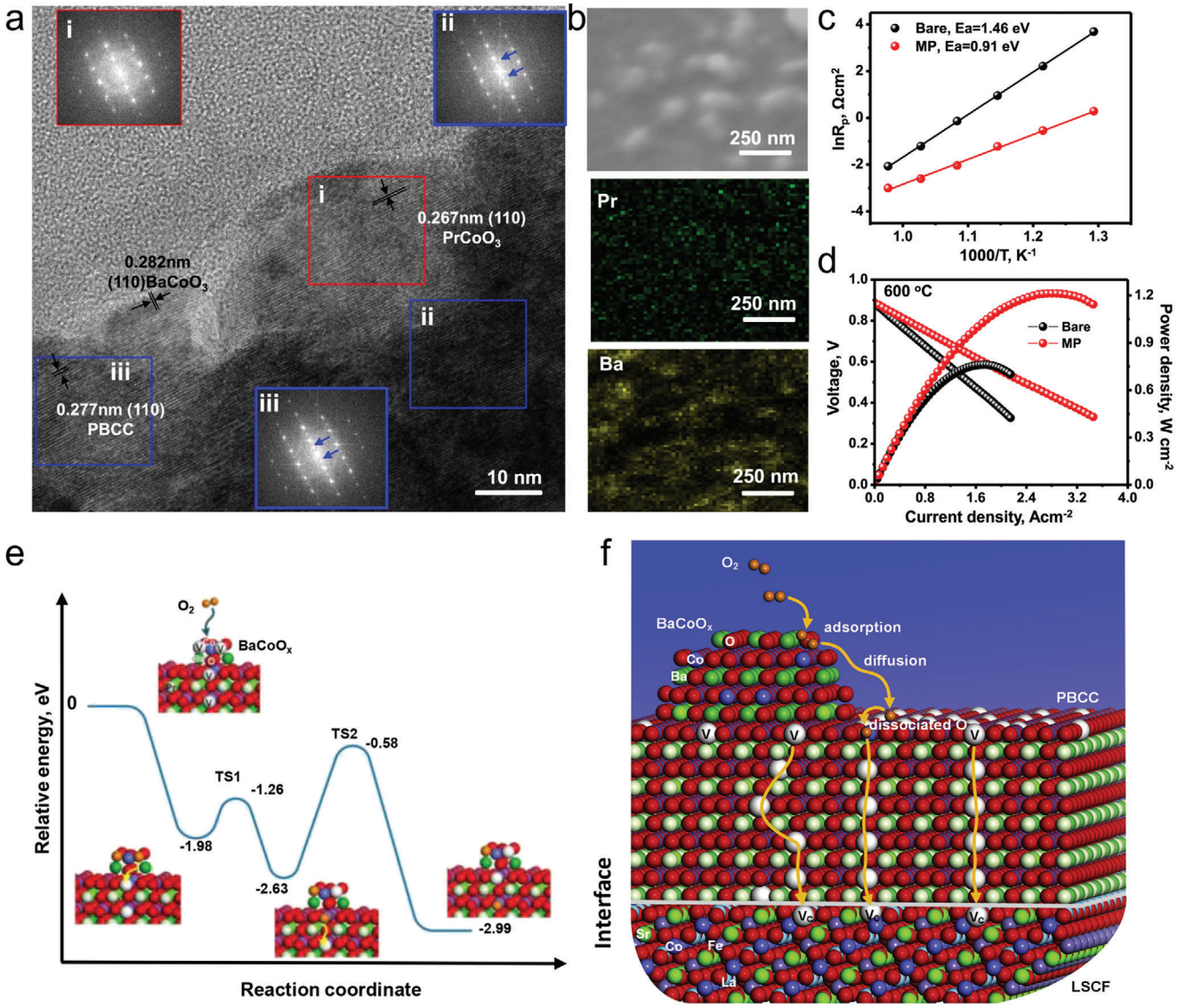

Figure 10. a) TEM image of PCO and BCO nanoparticles modified PBCC catalyst. Insets are FFT patterns of i) PC, ii), and iii) PBCC. b) SEM and element maps of PCO and BCO nanoparticles modified PBCC catalyst coated LSCF surface. c) Arrhenius plots of the polarization resistances of bare LSCF and PCO/BCO nanoparticles modified PBCC coated LSCF. d) *I–V* and *I–P* curves of Ni-$Gd_{0.2}Ce_{0.8}O_{1.9}$ fuel electrode-supported cell with LSCF and multi–*p*hase catalyst coated LSCF as air electrodes at 600 °C operate on H_2-3 vol% H_2O fuel. e) The energetics of ORR for BCO nanoparticle decorated PBCC. TS1 and TS2 represent the transition state of oxygen surface diffusion and bulk diffusion, respectively. f) Schematic diagram of the PCO/BCO nanoparticles modified PBCC coated LSCF air electrode. Reproduced with permission.[202] Copyright 2018, Elsevier Inc.

phase (Figure 11c,d). Consequently, the SCFN nanocomposite exhibited superior ORR activity compared to SF alone. An SDC-supported symmetric cell with the SCFN composite electrode exhibited drastically lower ASR values (0.072 Ω cm^2at 600 °C in the air) compared to the SF air electrode (0.24 Ω cm^2). A Ni-SDC fuel electrode-supported cell with the SCFN composite air electrode demonstrated a significantly higher maximum power density (0.98 W cm^{-2}) at 600 °C in H_2 fuel than a cell using the SF air electrode (0.65 W cm^{-2}). Additionally, the SCFN nanocomposite demonstrated high OER and ORR activity when used as an air electrode for reversible H-SOCs. In the SCFN nanocomposite, the RP-SF-based phase also promoted steam surface exchange (hydration) and proton conduction, while the NiO and CeO_2 nano-catalysts facilitated O_2 surface exchange and O^{2-} conduction from the surface to the major perovskite, thus enhancing the OER/ORR activity. A reversible H-SOC with SCFN as the air electrode achieved a high maximum power density of 531 mW cm^{-2} and an electrolysis current of −364 mA cm^{-2} at 1.3 V at 600 °C while maintaining excellent reversible durability of 120 h at 550 °C.[124]

Proton conducting phases can also be incorporated into O^{2-}/e^- mixed conductors using a one-pot synthesis approach. In this context, Shao et al. successfully designed a perovskite-based composite with a nominal composition of $BaCo_{0.7}Ce_{0.24}Y_{0.06}O_{3-\delta}$ (BCCY) using a one-pot synthesis method. During the calcination of the BCCY precursors

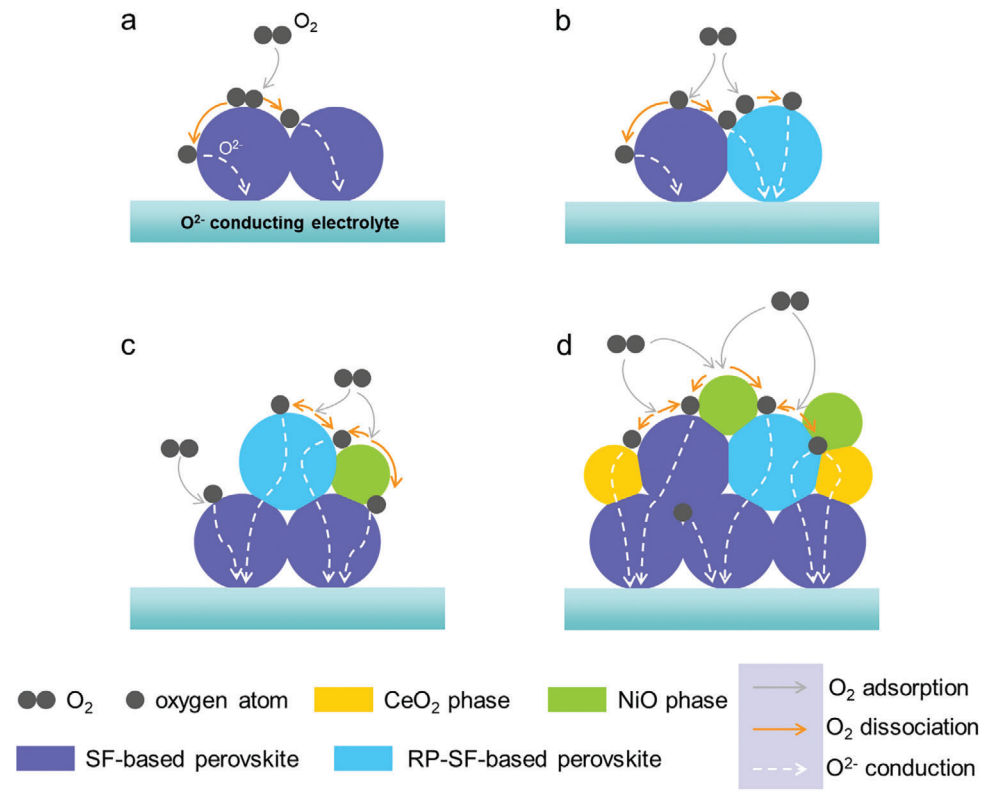

Figure 11. Schematic representation of ORR pathways on perovskite-based electrodes. a) Standard single-phase SF perovskite illustrating O_2 adsorption, dissociation, and O^{2-} ion conduction. b) Enhanced ORR process on SF/RP-SF (dual-phase) perovskite demonstrating improved oxygen reduction kinetics. c) ORR on NiO nanoparticle-modified SF/RP-SF perovskite shows further enhancement due to NiO catalytic activity. d) Composite electrode with both NiO and CeO_2 nanoparticles, exhibiting synergistic ORR promotion by leveraging the strengths of both catalysts. Reproduced with permission.[27] Copyright 2020, Wiley-VCH Verlag GmbH & Co. KGaA, Weinheim.

prepared through the sol-gel method, a dual-phase material was assembled in situ. This material comprised the mixed O^{2-}/e^- conducting material $BaCo_xCe_yY_zO_{3-\delta}$ (M-BCCY, Co-rich phase) and the mixed H^+/e^- conducting material $BaCe_xY_yCo_zO_{3-\delta}$ (P-BCCY, Ce-rich phase). Additionally, at temperatures specific to H-SOC operation (500–700 °C), a mixed O^{2-}/e^- conductor BCO material, also formed due to the partial decomposition of M-BCCY. During H-SOCs operation, the coexistence of M-BCCY and P-BCCY phases ensured triple $H^+/O^{2-}/e^-$ conductivity. Conversely, the presence of the BCO enhances oxygen adsorption/dissociation and electronic conduction, leading to superior ORR activity. In addition, the thermal expansion coefficients of M-BCCY and P-BCCY are 19.6×10^{-6} and 9.5×10^{-6} K^{-1}, respectively. The close contact between M-BCCY and P-BCCY effectively restrains BCCY's thermal expansion coefficient to 15.7×10^{-6} K^{-1}, ensuring operational stability. Symmetric cell tests showed that BCCY had better ORR activity than the state-of-the-art materials $Ba_{0.5}Sr_{0.5}Co_{0.8}Fe_{0.2}O_{3-\delta}$ and $BaCo_{0.4}Fe_{0.4}Zr_{0.1}Y_{0.1}O_{3-\delta}$. A Ni-BZCYYb fuel electrode-supported H-SOC achieved a high maximum power density of 0.99 W cm^{-2} at 650 °C while maintaining durability for 812 hours at 550 °C.[52] Tong et al. proposed a perovskite-based dual-phase nanocomposite, with nominal composition $BaCe_{0.4}Fe_{0.4}Co_{0.2}O_{3-\delta}$, combining $BaCe_xCo_yFe_zO_{3-\delta}$, a Ce-rich phase capable of mixed H^+/e^- conductivity, and $BaCo_xFe_yCe_zO_{3-\delta}$, a Co/Fe-rich phase capable of mixed O^{2-}/e^- conductivity. The resulting $BaCe_{0.4}Fe_{0.4}Co_{0.2}O_{3-\delta}$ air electrode showed excellent performance; for instance, the button H-SOC with $BaCe_{0.4}Fe_{0.4}Co_{0.2}O_{3-\delta}$ as air electrode had a low polarization resistance of 0.075 Ω cm^2.[204]

The works of Shao and Tong underscore several critical challenges in developing air electrodes for H-SOCs. Early attempts directly employed O^{2-}/e^- mixed conductors as air electrodes. However, the lack of proton conductivity, which is essential for H-SOCs, restricted ORR reaction zones to the electrode-electrolyte interface (**Figure 12a,b**). Using H^+ conductors with low e^- conductivity also proved limiting, confining ORR reactions to the electrode surface (Figure 12c). While some researchers explored introducing proton conductors via infiltration or mechanical mixing, these composite air electrodes suffered from poor contact under H-SOC conditions. Moreover, large grain size and uneven phase distribution reduced the number of active sites, leading to low and unstable cathodic activity (Figure 12d). To overcome these limitations, Shao and Tong proposed an in situ assembled triple-conducting nanocomposite air electrode. This design addresses the need for high triple conductivity, abundant ORR active sites, and optimal multi–*p*hase contact, promising superior activity and robust stability (Figure 12e).[52]

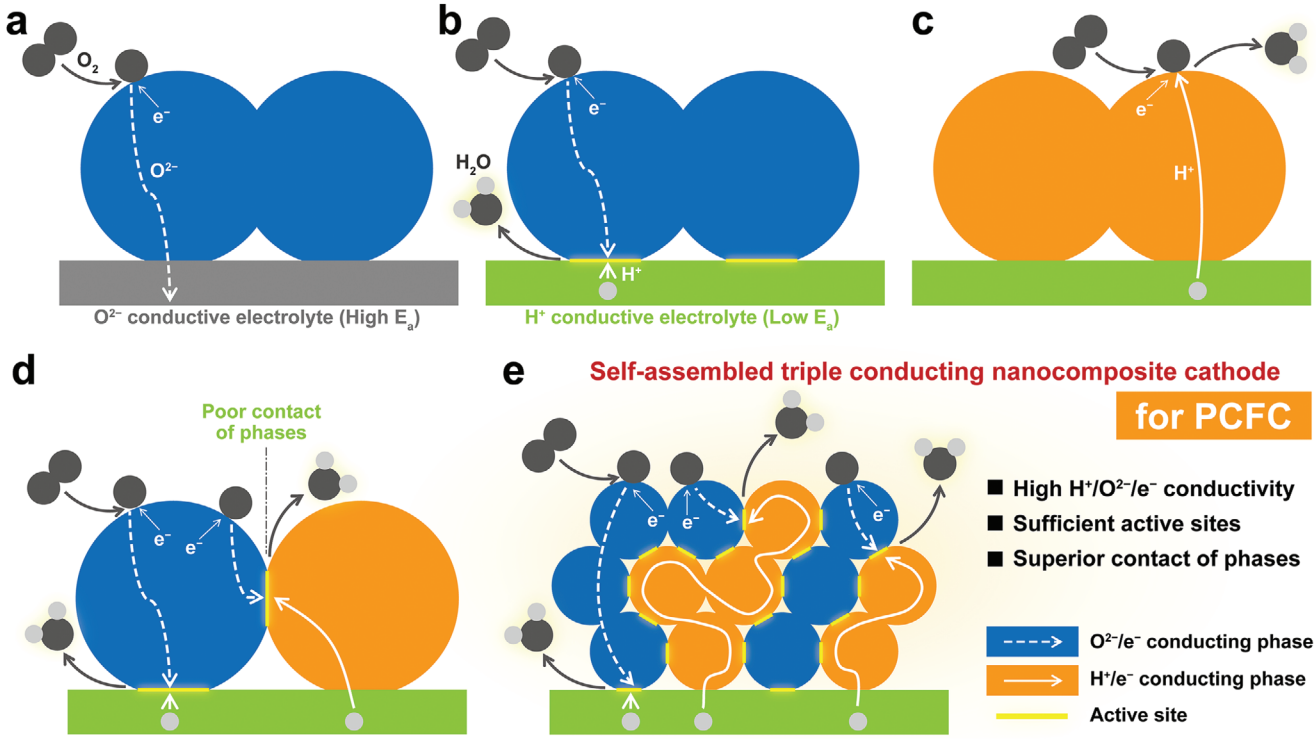

Figure 12. Comparative schematics of air electrode configurations in SOCs. a) O-SOC with O^{2-}/e^- conducting air electrode. b) H-SOC with e^- conducting air electrode. c) H-SOC with H^+/e^- conducting air electrode. d) Mixed ion and electron conductor with poor phase contact. e) In situ assembled nanocomposite air electrode for H-SOCs, featuring high $H^+/O^{2-}/e^-$ conductivity, ample active sites, and optimal phase contact for enhanced performance. Generally, O^{2-} conductors are characterized by higher activation energy than H^+ conductors. Reproduced with permission.[52] Copyright 2019, Elsevier Inc.

4.2.2. Segregation

Surface cation segregation in perovskites can be induced by various mediators, including H_2/O_2, water vapor, and oxides (e.g., SrO, BaO), especially at high temperatures. This process leads to secondary phase formation. By carefully controlling segregation, researchers can create beneficial secondary phases that enhance the material's catalytic activity toward oxygen reactions. Surface decoration offers a powerful tool for tailoring localized chemistry, driving cation segregation, and promoting the development of these advantageous secondary phases. Three primary types of surface segregation have been extensively investigated: 1) H_2/O_2-mediated, where the presence of these two species alters the surface structure, inducing cation segregation; 2) oxide-mediated, where introducing specific oxides (e.g., SrO, BaO) triggers segregation, generating desirable secondary phases; and 3) water-mediated, where water vapor modifies the surface chemistry, thus influencing the segregation process.

H_2/O_2-Mediated Surface Segregation: H_2/O_2-mediated surface segregation process can be used to create metal nanocatalysts with strong particle-substrate interaction, which enhances catalytic activity and durability.[205] In a recent study, Jung et al. developed a novel perovskite air electrode modified with socketed Ag nanoparticles, using a $BaCo_{0.8}Nb_{0.1}Ta_{0.1}O_{3-\delta}$ (BCNT) precursor that was doped with Ag to make up $Ba_{0.95}Ag_{0.05}Co_{0.8}Nb_{0.1}Ta_{0.1}O_{3-\delta}$ (BACNT) and then exsolved in situ during a pre-processing step conducted in H_2/Ar mixture at 320 °C (**Figure 13a**). The resulting Ag nanoparticles modified $Ba_{0.95}Ag_{0.05}Co_{0.8}Nb_{0.1}Ta_{0.1}O_{3-\delta}$ (e-BACNT), facilitating the oxygen surface exchange rate and leading to lower polarization resistances (0.020 and 0.098 Ω cm^2 at 650 and 550 °C, respectively) compared to pristine BCNT (0.032 and 0.098 Ω cm^2) (Figure 13b,c). A button cell using the modified electrode was stable during a 225 h stability test with no significant degradation (Figure 13d), indicating the excellent anti-sintering capability of the exsolved Ag nano-catalysts (Figure 13e).[205]

In another study, Zhu et al. synthesized a high-performance air electrode by incorporating Ag nanoparticles into $Sr_{0.95}Nb_{0.1}Co_{0.9}O_{3-\delta}$ perovskite. The Ag nanoparticles were formed by processing $Sr_{0.95}Ag_{0.05}Nb_{0.1}Co_{0.9}O_{3-\delta}$ in a 10 vol% H_2/Ar atmosphere at 320 °C. The presence of Ag enhanced performance and demonstrated significantly better ORR activity of the Ag-containing compound relative to unmodified $Sr_{0.95}Nb_{0.1}Co_{0.9}O_{3-\delta}$. In an SDC-supported symmetric cell, the nano-Ag-modified $Sr_{0.95}Nb_{0.1}Co_{0.9}O_{3-\delta}$ electrode exhibited lower ASR values of 0.037 and 0.21 Ω cm^2 at 600 and 500 °C, respectively, in air, compared to pristine $Sr_{0.95}Nb_{0.1}Co_{0.9}O_{3-\delta}$ (0.056 and 0.36 Ω cm^2).[206] Building upon the work of Zhu et al. on Ag exsolution, the rationale behind the excellent anti-sintering capability of socketed Ag nanoparticles on $Sr_{0.95}Nb_{0.1}Co_{0.9}O_{3-\delta}$ is elucidated. To quantify the contact strength between the Ag nanoparticles and the $Sr_{0.95}Nb_{0.1}Co_{0.9}O_{3-\delta}$ support, Zhu et al. employed adhesion energy (E_{adh}) as a proxy.[207–209] A high E_{adh}

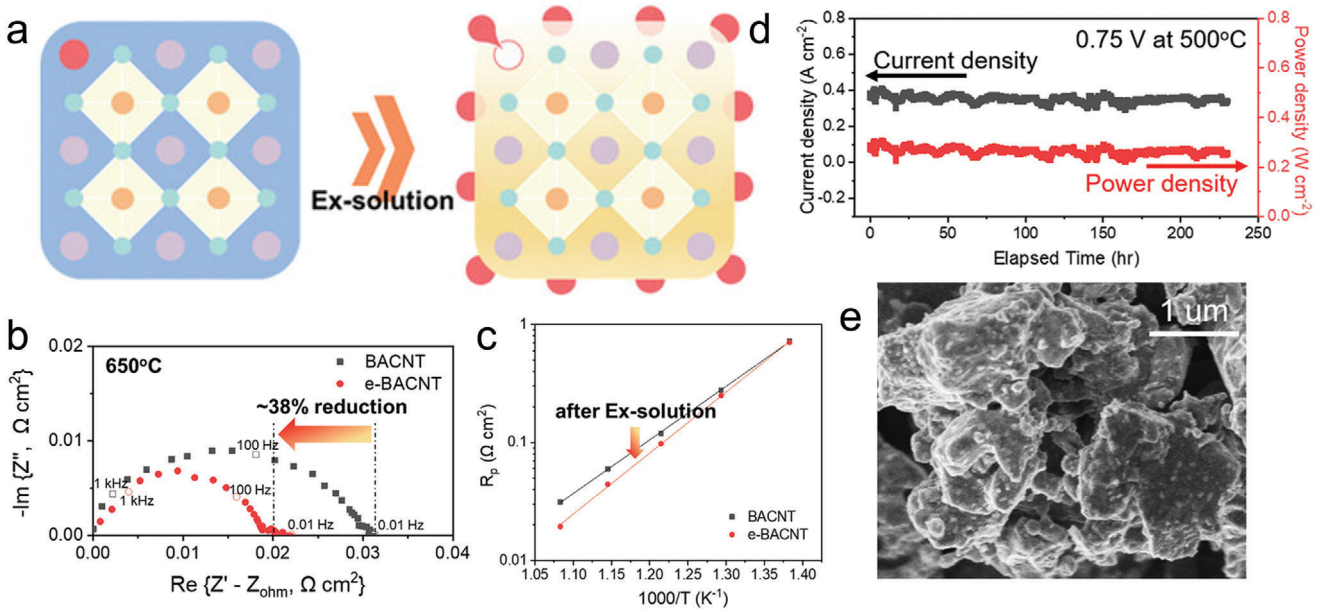

Figure 13. a) Schematics of exsolution process. b) EIS profiles and c) Arrhenius plots of the polarization resistances of SDC-supported symmetric cells with Ag nanoparticles modified BACNT (e-BACNT) and pristine BCNT as electrodes. d) Operational stability of Ni-SDC fuel electrode-supported cell with e-BACNT as air electrode at 500 °C. e) Surface morphology of e-BACNT air electrode after >225 h of operation. Reproduced with permission.[205] Copyright 2020, Wiley-VCH Verlag GmbH & Co. KGaA, Weinheim.

value signifies a strong metal-support interaction, implying robust bonding between the Ag and $Sr_{0.95}Nb_{0.1}Co_{0.9}O_{3-\delta}$ support. The E_{adh} correlates almost linearly with the negative heat formation of the oxide support per mole of oxygen ($-\Delta H_{f,OxSup}$), and as $-\Delta H_{f,OxSup}$ decreases, the E_{adh} increases.[209] For perovskite, average metal-oxygen bond energy (ABE) equals $\Delta H_{f,OxSup}$.[210] In this study, the authors compared the $\Delta H_{f,OxSup}$ of $Sr_{0.95}Nb_{0.1}Co_{0.9}O_{3-\delta}$ with that of CeO_2, since socketed Ag nanoparticles on CeO_2 surfaces have excellent anti-sintering capability.[207–209,211] They found that the $-\Delta H_{f,OxSup}$ of $Sr_{0.95}Nb_{0.1}Co_{0.9}O_{3-\delta}$ was much lower than that of CeO_2, suggesting stronger adhesion between Ag nanoparticles and $Sr_{0.95}Nb_{0.1}Co_{0.9}O_{3-\delta}$. In addition, the $Sr_{0.95}Nb_{0.1}Co_{0.9}O_{3-\delta}$ showed high oxygen vacancy content, which may also play a key role in determining adhesion energies on the basis of previous research that oxygen vacancies stabilize metal nanoparticles' adsorption on various oxides.[212]

Perovskite materials can be engineered to generate nanocatalysts through a two-step in situ process: exsolution followed by re-oxidation. First, active elements are doped into the perovskite lattice during synthesis. Under high temperatures and a reducing atmosphere (often containing H_2), these elements exsolve as metal nanoparticles onto the surface. Subsequently, switching to an oxidizing atmosphere transforms the exsolved metal nanoparticles into oxide nanoparticles. These surface-enriched oxide nanoparticles can enhance oxygen surface reaction kinetics, potentially improving catalytic performance. Under certain air electrode conditions, exsolved metal nanoparticles may spontaneously oxidize, forming oxide nanoparticles that enhance O_2 surface reaction kinetics by providing additional oxygen adsorption sites. For example, Shen et al. developed a Pd nanoparticle-modified perovskite electrode by reducing $LaCo_{0.67}Fe_{0.3}Pd_{0.03}O_{3-\delta}$ in 10 vol% H_2—Ar at 800 °C. The exsolved Pd oxidized to PdO_x during symmetric cell testing (800 °C, air atmosphere), significantly enhancing ORR activity. This modification resulted in a lower polarization value (0.35 Ω cm^2) compared to the $LaCo_{0.7}Fe_{0.3}O_{3-\delta}$-infiltrated SDC air electrode (0.99 Ω cm^2).[160] Similarly, Yang et al. demonstrated that re-oxidizing exsolved metal nanoparticles into oxides can activate the perovskite surface and boost ORR activity. After reducing $SrFe_{0.85}Ti_{0.1}Ni_{0.05}O_{3-\delta}$ in 10 vol% H_2—Ar, they calcined it in air at 600 °C. This oxidized the exsolved Ni into NiO nanoparticles, enriching them on the $SrFe_{0.85}Ti_{0.1}Ni_{0.05}O_{3-\delta}$ surface. Symmetric cell tests of $SrFe_{0.9}Ti_{0.1}O_{3-\delta}$ and $SrFe_{0.85}Ti_{0.1}Ni_{0.05}O_{3-\delta}$ electrodes demonstrated that the NiO nanoparticles primarily enhance the surface reaction kinetics, contributing to lower ASR values.[28]

Oxide-Mediated Surface Segregation: Oxides also play a significant role as segregation mediators. It has been observed that oxides enriched on the surface, can effectively inhibit the segregation of the same cations in the substrate material. However, intriguingly, these surface-modified materials can promote the segregation of other cations within the substrate. **Figure 14** illustrates key results from a study by Li et al. in which a $Sr(NO_3)_2$ solution was used to deposit SrO on the surface of $La_{0.6}Sr_{0.4}CoO_{3-\delta}$. The introduced Sr^{2+} exhibited higher mobility than those within the $La_{0.6}Sr_{0.4}CoO_{3-\delta}$ bulk. This greater mobility allows them to occupy surface sites more prone to segregation (e.g., defects, grain boundaries, or dislocations), ultimately inhibiting the flux of Sr toward the surface. Preventing Sr^{2+} segregation promoted La^{3+} and Co^{3+} migration to the surface. There, these cations reacted with the infiltrated SrO, forming nano-sized $(La,Sr)CoO_{3-\delta}$, which enhanced electronic and oxygen-ion conduction and led to a nearly 30 times lower electrode resistance than pristine $La_{0.6}Sr_{0.4}CoO_{3-\delta}$.[149]

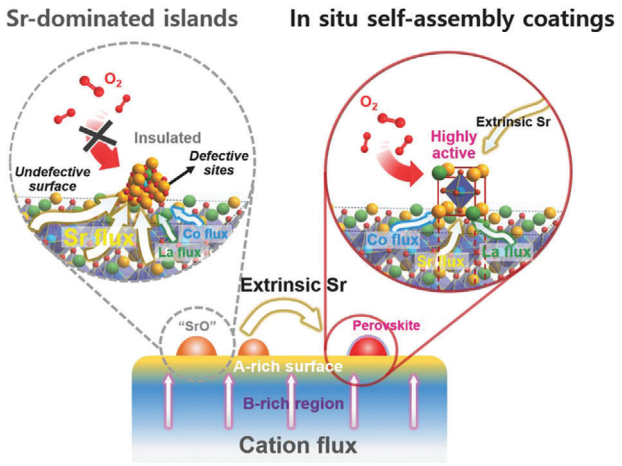

Figure 14. Comparative schematic illustrating the surface modification of $La_{0.6}Sr_{0.4}CoO_{3-\delta}$ perovskite. Sr-dominated islands with undefective surface and insulated defective sites due to SrO segregation (Left); An in situ assembled coating on the $La_{0.6}Sr_{0.4}CoO_{3-\delta}$ surface, showing extrinsic Sr integration into the perovskite structure, resulting in a highly active surface for oxygen reduction reactions with enhanced cation flux dynamics (Right). Reproduced with permission.[149] Copyright 2018, Wiley-VCH Verlag GmbH & Co. KGaA, Weinheim.

Xia et al. employed a similar strategy, infiltrating $Sr(NO_3)_2$ onto the surface of $La_{0.8}Sr_{0.2}FeO_{3-\delta}$ and subsequently calcining it at a high temperature (800 °C). This process resulted in the formation of a $(La,Sr)_2FeO_4$-decorated $La_{0.8}Sr_{0.2}FeO_{3-\delta}$ heterostructured electrode. Oxygen chemical surface exchange coefficient measurements were increased by an order of magnitude relative to bare $La_{0.8}Sr_{0.2}FeO_{3-\delta}$. The lattice mismatch between the $(La,Sr)_2FeO_4$ and $La_{0.8}Sr_{0.2}FeO_{3-\delta}$ phases resulted in tensile strain. In this heterostructure, the O_2 adsorption and oxygen vacancy formation were more favored than pristine $La_{0.8}Sr_{0.2}FeO_{3-\delta}$ because of weakened in-plane Fe-O bonds,[213,214] thus enhancing ORR activity.[215]

Chen et al. studied oxide evaporation as an alternative method to infiltration for introducing beneficial oxides onto perovskite air electrode surfaces. They developed a $PrNi_{0.5}Mn_{0.5}O_{3-\delta}$ (PNM) nanocomposite air electrode via a one-pot in situ assembly process, which resulted in a PNM primary phase with surface-enriched PrOx nanoparticles. During the fabrication and operation of a Ni-BZCYYb|BZCYYb|PNM cell, BaO vapor diffused and deposited onto the PNM electrode. The formed BaO then reacted with both PNM and the PrO_x nanoparticles during operation. This reaction formed additional Ba-doped PNM nanoparticles and proton-conducting $BaPrO_{3-\delta}$ (BPO) nanoparticles, respectively (**Figure 15**a,b). The oxygen-vacancy-rich PrO_x nanoparticles facilitated oxygen surface exchange, while the PNM phase promoted oxygen transfer within the electrode (Figure 15b). Consequently, during cell operation, the surface-enriched PNM/PrO_x composite gradually transformed into a BPO/Ba-doped PNM composite, leading to an increase in power density (Figure 15c). This surface modification demonstrably enhanced performance as evidenced by a PPD increase (H-SOC operation) from 0.66 to 0.79 W cm^{-2} at 700 °C with H_2 fuel (Figure 15d).[216]

Steam-Mediated Surface Segregation: Kim et al. proposed a water-mediated surface in situ assembly strategy to enhance ORR activity. These authors used steam (3 vol% H_2O-Air) at 600 °C to segregate BCO toward the surface of PBCC. The presence of BCO enhanced O_2 adsorption, thus improving ORR activity (**Figure 16**a). In situ Raman characterization revealed the formation of surface hydroxyl groups and proton-elongated superoxol on the PBCC phase after steam treatment. These species are implicated in a significant ORR pathway under wet air conditions (Figure 16b,c). Density functional theory calculations further supported this mechanism, indicating that these surface modifications facilitated the diffusion of dissociated oxygen atoms into the sublattice, further enhancing ORR activity (Figure 16d). Symmetric cell tests demonstrated the benefits of steam treatment as PBCC electrodes decorated with BCO nanoparticles achieved lower ASR and activation energy in wet air compared to dry air (Figure 16e,f). Notably, conventional LSCF electrodes exhibited the opposite trend. An O-SOC (Ni-YSZ|ScSZ|SDC|PBCC) with the steam-treated PBCC air electrode achieved a significantly higher maximum power density in wet air (1.46 W cm^{-2}) compared to dry air (0.94 W cm^{-2}) (Figure 16g).[217]

Zhou et al. employed PBCC material as an H-SOC air electrode. Under high-temperature humidified H-SOC conditions, they observed in situ exsolution of BCO nano-catalysts, which enriched the PBCC surface and significantly enhanced OER activity. The resulting H-SOC achieved (at 600 °C) a maximum power density of 1.06 W cm^{-2} in fuel cell mode and a current density of 1.51 A cm^{-2} at 1.3 V in electrolysis mode. Density functional theory calculations were used to compute the free energy of various OER steps, suggesting that the BCO promotes water adsorption and dissociation ($H_2O \rightarrow OH^* + H^*$; $OH^* \rightarrow O^* + H^*$), while PBCC facilitates oxygen formation ($O^* - 2e^- \rightarrow 1/2O_2$) and desorption. These two contributions synergistically enhance OER activity.[46]

Pei et al. developed $Ba_{0.9}Co_{0.7}Fe_{0.2}Nb_{0.1}O_{3-\delta}$ (BCFN) as a reversible H-SOC air electrode. During operation, a reaction with steam transformed it into an Nb-deficient BCFN nano-perovskite. This transformation generated additional ORR- and OER-active regions, significantly boosting catalytic activity (**Figure 17**a). A button cell utilizing this composite delivered a high PPD of 1.7 W cm^{-2} in fuel cell mode (Figure 17b) and a current density of 2.8 A cm^{-2} at 1.3 V in electrolysis mode (Figure 17c) at 650 °C. Notably, the same cell demonstrated stability in both fuel cell (≈112 h) and electrolysis (≈220 and ≈380 h at constant current densities of −1.0 and −0.5 A cm^{-2}, respectively) modes (Figure 17d,e).[218] Similarly, Xu et al. used $PrBaCo_{1.6}Fe_{0.2}Nb_{0.2}O_{5+\delta}$ as a reversible H-SOC air electrode. During H-SOC operation, it reacted with water vapor at 650 °C, resulting in the in situ formation of Nb-deficient $PrBaCo_{1.6}Fe_{0.2}Nb_{0.2-x}O_{5+\delta}$ nano-catalysts on the $PrBaCo_{1.6}Fe_{0.2}Nb_{0.2}O_{5+\delta}$ surface. These nanoparticles enhanced OER and ORR activity. An H-SOC using this composite air electrode reached a high PPD of 1.059 W cm^{-2} in fuel cell mode, a current density of 2.148 A cm^{-2} at 1.3 V in electrolysis mode, and exhibited reversible durability between 0.5 and −0.5 A cm^{-2} for 200 h.[219] In both studies, the exsolved Nb-deficient perovskite possessed a higher oxygen vacancy concentration than the substrate due to Nb deficiency.

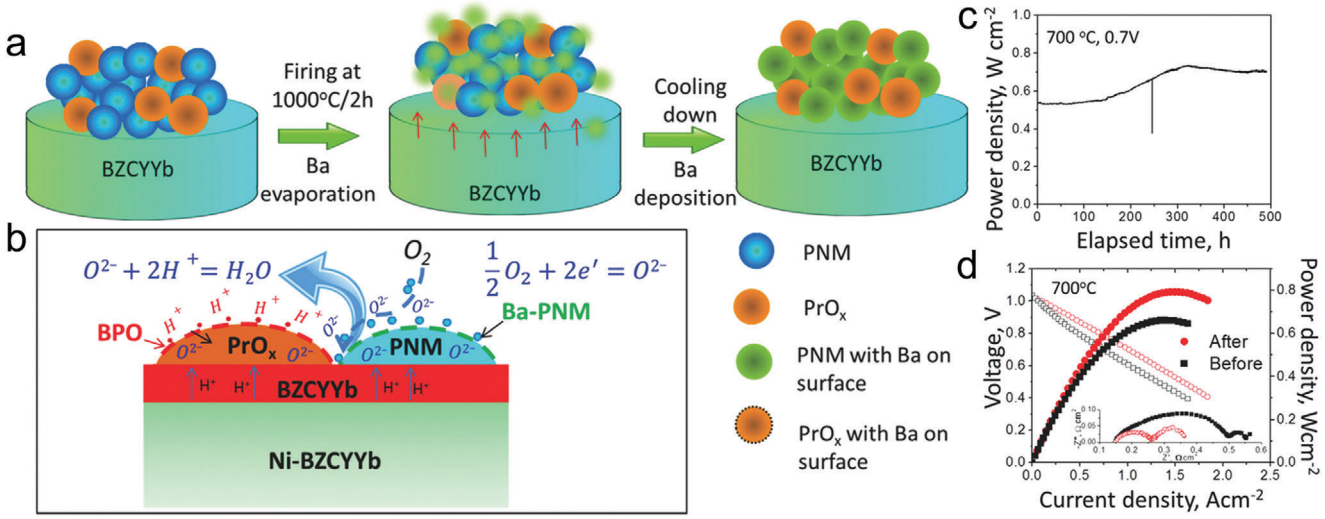

Figure 15. Schematic illustration of key processes in the H-SOC with a Ba-modified PNM nanocomposite air electrode: a) Ba evaporation and interaction with the PNM composite, b) electrode reaction mechanism during H-SOC operation, c) power density changes resulting from Ba-PNM interaction, and d) cell performance and stability, including *I–V* and *I–P* curves and EIS data before and after operational testing. Reproduced with permission.[216] Copyright 2017, Wiley-VCH Verlag GmbH & Co. KGaA, Weinheim.

Beyond perovskite segregation, water vapor can also induce surface segregation of simple oxides (e.g., barium oxide)[220] and metals (e.g., silver),[221] thus enhancing the electrocatalytic activity of perovskites. Jung et al. demonstrated that water vapor can modulate exsolution in triple-conducting oxides containing readily reducible metals. The reaction between water vapor and the oxide ($H_2O + 2O_O^{\times} + 2h^{\cdot} \leftrightarrow 2OH_O^{\cdot} + \frac{1}{2}O_2$) facilitates exsolution by removing holes ($h^{\cdot}$) in proximity to metal cations, promoting their reduction and migration to the oxide surface. The authors studied Ag-doped $BaCo_{0.4}Fe_{0.4}Zr_{0.1}Y_{0.1}O_{3-\delta}$ ($Ba_{0.95}Ag_{0.05}Co_{0.4}Fe_{0.4}Zr_{0.1}Y_{0.1}O_{3-\delta}$), subjecting it to humidified air at 650 °C. This treatment resulted in the exsolution of Ag nanoparticles, leading to a significant enhancement in ORR activity of the air electrode. An H-SOC employing the Ag-modified air electrode achieved a peak power density of 1.20 W cm^{-2} at 650 °C. This value represents a nearly 1.47-fold improvement compared to the cell utilizing $BaCo_{0.4}Fe_{0.4}Zr_{0.1}Y_{0.1}O_{3-\delta}$ as the air electrode.[220]

Jung et al. further proposed a method for enhancing exsolution by doping $BaCo_{0.4}Fe_{0.4}Zr_{0.1}Y_{0.1}O_{3-\delta}$ with monovalent alkali metal cations (M^+, M = K). This approach involves incorporating 5% K^+ to create $K_{0.05}Ba_{0.95}Co_{0.4}Fe_{0.4}Zr_{0.1}Y_{0.1}O_{3-\delta}$. The subjection of the as-synthesized $K_{0.05}Ba_{0.95}Co_{0.4}Fe_{0.4}Zr_{0.1}Y_{0.1}O_{3-\delta}$ powder to humidified air (3 vol% H_2O) at 600 °C for 12 h facilitates the in situ exsolution and surface enrichment of BaO_x nanoparticles on the $K_{0.05}Ba_{0.95}Co_{0.4}Fe_{0.4}Zr_{0.1}Y_{0.1}O_{3-\delta}$ perovskite. A-site acceptor doping with K^+ accelerated the formation of BaO_x exsolution due to their stronger basicity compared to Ba^{2+}. This increased basicity weakens the interaction between Ba and the A-site, favoring BaO_x segregation upon exposure to water vapor and oxygen.[222] While exsolved BaO_x nanoparticles might hinder oxygen reduction reaction sites due to their blockage of charge-transfer pathways, they can concurrently promote acid-base reactions, particularly hydration. This facilitation of proton conduction can enhance the overall performance of the H-SOC. Consequently, an H-SOC with $K_{0.05}Ba_{0.95}Co_{0.4}Fe_{0.4}Zr_{0.1}Y_{0.1}O_{3-\delta}$ as air electrode showed a peak power density of 1.65 W cm^{-2} in fuel cell mode, and a current density of −6.5 A cm^{-2} at 1.3 V in electrolysis mode.[221]

4.2.3. Phase Reaction

Composite electrodes are typically prepared by blending single-phase materials followed by high-temperature calcination. While this process can promote cation exchange or secondary phase formation, thus enhancing electrochemical performance and durability, the intricate phase interactions often make outcomes difficult to predict.

During H-SOC fabrication, Shao et al. observed cation exchange between $BaZr_{0.1}Ce_{0.7}Y_{0.2}O_{3-\delta}$, a protonic ceramic electrolyte, and the $PrBaCo_2O_{5+\delta}$ (PBC), an air electrode. To promote adhesion, PBC was calcined at 950 °C with the $BaZr_{0.1}Ce_{0.7}Y_{0.2}O_{3-\delta}$ electrolyte, leading to Y and Co diffusion. This process led to Co-doped $BaZr_{0.1}Ce_{0.7}Y_{0.2}O_{3-\delta}$ and Y-doped PBC. Co-doping lowered $BaZr_{0.1}Ce_{0.7}Y_{0.2}O_{3-\delta}$'s ionic conductivity; while pure $BaZr_{0.1}Ce_{0.7}Y_{0.2}O_{3-\delta}$ demonstrated conductivities of 0.014 S cm^{-1} (humidified air) and 0.01 S cm^{-1} (H_2) at 600 and 500 °C, respectively, the Co-doped variant exhibited lower conductivities of 0.0076 S cm^{-1} and 0.0077 S cm^{-1}, respectively. In contrast, Y-doped PBC had enhanced ORR activity. A $BaZr_{0.1}Ce_{0.7}Y_{0.2}O_{3-\delta}$-supported symmetric cell with YPBC electrodes displayed a lower polarization resistance (0.58 Ω cm^2) compared to PBC (0.76 Ω cm^2) in humidified air at 600 °C.[223]

Liu et al. controlled phase transformation during the high-temperature calcination of a $BaZr_{0.1}Ce_{0.7}Y_{0.2}O_{3-\delta}$-SSC air electrode composite. XRD analysis revealed that reactions between the proton conductor $BaZr_{0.1}Ce_{0.7}Y_{0.2}O_{3-\delta}$ and the mixed O^{2-}/e^- conductor SSC generated $BaCoO_{3-\delta}$ (a mixed O^{2-}/e^-

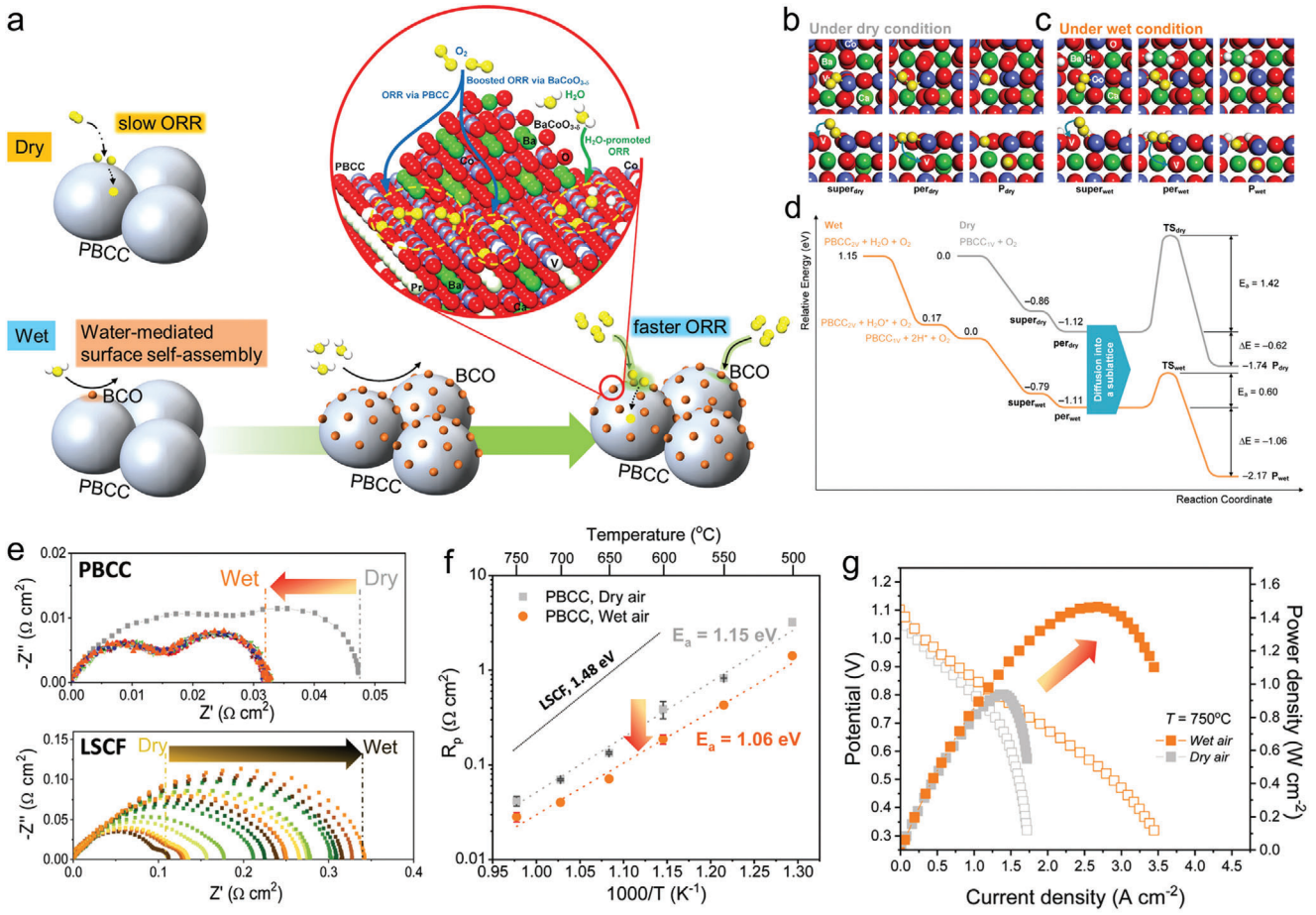

Figure 16. a) Schematic of ORR in water-mediated surface in situ assembled PBCC and untreated PBCC. Density functional theory-based clarifies the surface species adsorbed on PBCC(010) under b) dry and c) wet atmospheres. d) Schematic of the energetics of ORR on PBCC(010) under dry and wet atmospheres. e) EIS profiles of the symmetric cells with PBCC and LSCF as electrodes measured under 3 vol% H_2O-air at 750 °C. f) Arrhenius plot of the electrode impedance of PBCC electrodes under air and 3 vol% H_2O-air. g) *I–V* and *I–P* curves of the PBCC air electrode-based O-SOC under dry and wet air at 750 °C. Reproduced with permission.[217] Copyright 2017, Royal Society of Chemistry.

conductor) and $SmZrO_{3-\delta}$ (a new proton conductor). These newly formed phases enhanced ORR activity by promoting O_2 adsorption/dissociation and proton conductivity. An H-SOC using the $BaZr_{0.1}Ce_{0.7}Y_{0.2}O_{3-\delta}$-SSC composite as air electrode achieved impressive power densities of 725 mW cm^{-2} at 700 °C and 445 mW cm^{-2} at 600 °C in H_2 fuel.[224] Interestingly, too-high calcination temperatures increased $SmZrO_{3-\delta}$ content, introducing higher interfacial resistances due to its low electronic conductivity, ultimately hampering performance.

Zhang et al. developed a strategy to match the thermal expansion coefficient of typical electrodes to that of YSZ. They achieved this by mechanically mixing the air electrode material $SrNb_{0.1}Co_{0.9}O_{3-\delta}$ (SNC) with the negative-thermal-expansion material $Y_2W_3O_{12}$ (YWO), followed by calcination of the mixture at 800 °C. This calcination process induced a phase reaction between SNC and YWO, resulting in a composite (*c*-SYNC) consisting of A-site deficient $Sr_x(Y_y(Nb_{0.1}Co_{0.9})_{1-y})O_{3-\delta}$ (SYNC), $SrWO_4$ (SWO), and YWO. The SWO phase, well-connected to both SYNC and YWO, effectively suppressed thermal expansion. This resulted in a composite with a thermal expansion coefficient (12.9×10^{-6} K^{-1}) closely matching that of YSZ ($11.2–12.3 \times 10^{-6}$ K^{-1}). During the high-temperature (800 °C) preparation process, a cation exchange occurred: the yttrium from YWO partially substituted for Co/Nb on the B-site of SNC. Simultaneously, Sr from SNC reacted with tungstate W from YWO, forming SYNC and SWO (**Figure 18a–c**). The presence of A-site deficiencies in SYNC promoted the creation of oxygen vacancies. This directly boosted ORR activity and resulted in a more durable composite air electrode. The electrode's superior performance is demonstrated by its significantly lower polarization resistances compared to pristine SNC (Figure 18d–f). The c-SYNC composite exhibited remarkable durability during rapid thermal cycling tests. Even after 40 cycles (90 h) between 300 and 600 °C, it showed minimal increases in polarization and ohmic resistances, while the pristine SNC electrode degraded significantly. This durability is evident in post-test imaging, where extensive cracking is seen in SNC (Figure 18g) but not in *c*-SYNC (Figure 18h). Figure 18i,j explains this resilience, highlighting c-SYNC's reduced thermal expansion coefficient and the protective role of the SWO phase.[30]

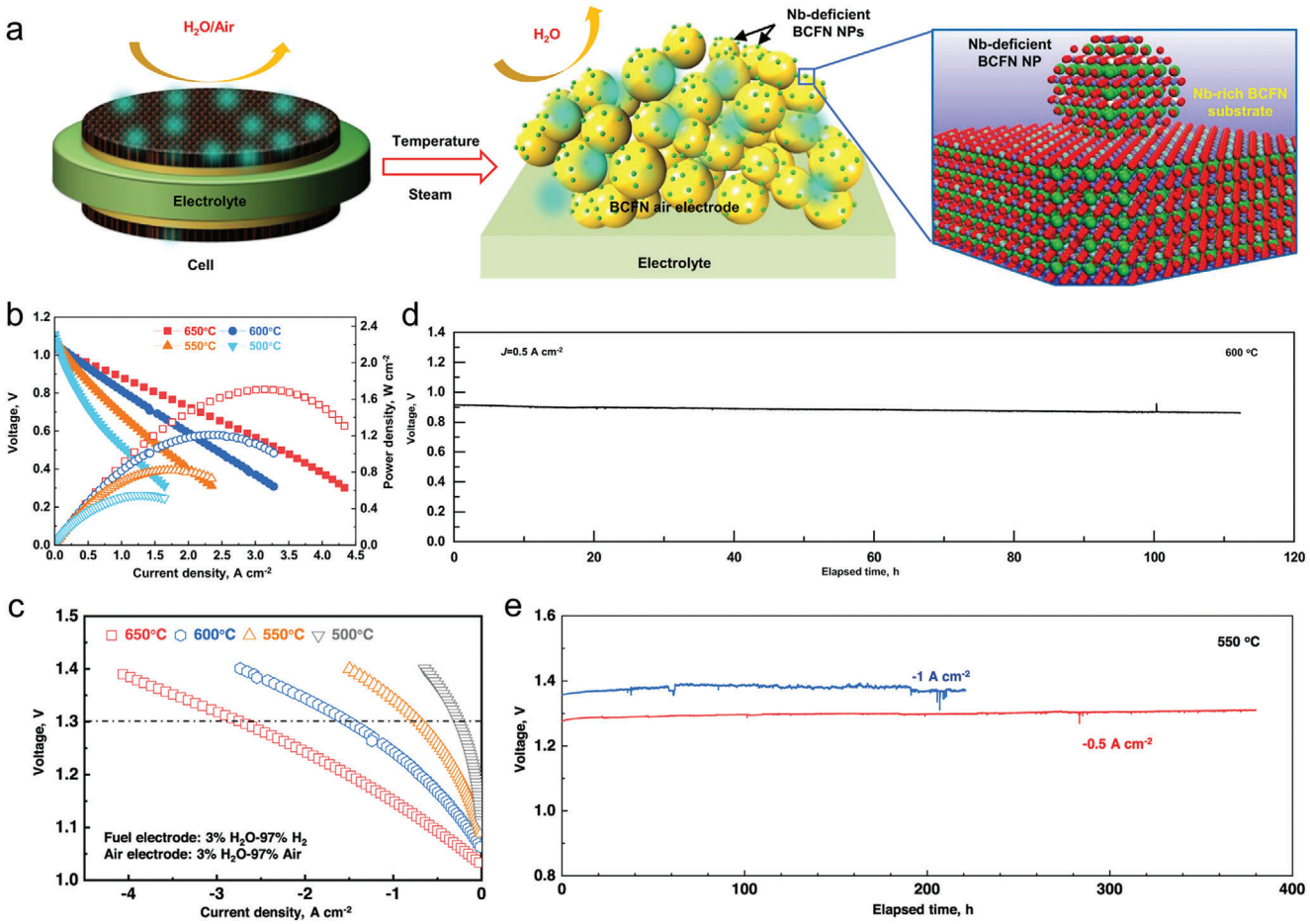

Figure 17. BCFN air electrode transformation and H-SOC performance. a) Schematic illustrating the formation of Nb-deficient BCFN nanoparticles on BCFN. b) *I–V* and *I–P* curves of H-SOC with the composite air electrode operating on H_2 fuel. c) H-SOC *I–V* curves during electrolysis operation. d) Operational stability in fuel cell mode. e) Operational stability in electrolysis mode. Reproduced with permission.[218] Copyright 2022, Nature Publishing Group.

4.2.4. Dynamic Cation Exchange

Dynamic cation exchange offers a powerful tool to optimize SOC electrode materials for thermal expansion, stability, and performance.[31,225] Rosseinsky et al. elegantly demonstrated this principle. By substituting W into the B-site of $Ba_{0.5}Sr_{0.5}Co_{0.8}Fe_{0.2}O_{3-\delta}$ ($Ba_{0.5}Sr_{0.5}(Co_{0.8}Fe_{0.2})_{0.6875}W_{0.3125}O_{3-\delta}$), they created a composite featuring a single perovskite phase $Ba_{0.5}Sr_{0.5}Co_{0.589(10)}Fe_{0.354(9)}W_{0.056(3)}O_{2.304(21)}$ and a B-site ordered double perovskite phase $BaSrCo_{0.847(12)}Fe_{0.260(22)}W_{0.891(17)}O_6$ (**Figure 19**a–c). Under O-SOC conditions, W migrated from the double into the single perovskite, boosting chemical stability. Additionally, the double perovskite phase acted as a mechanical support against sintering and, due to its lower thermal expansion coefficient, helped the composite match the electrolyte's thermal expansion. This single/double perovskite system delivered significantly improved performance. An SDC-supported cell using this composite air electrode showed polarization resistance as low as 0.034 Ω cm^2 at 650 °C, along with an exceptionally low degradation rate (1.6×10^{-6} Ω cm^2 min^{-1}) (Figure 19d). Crucially, unlike standard $Ba_{0.5}Sr_{0.5}Co_{0.8}Fe_{0.2}O_{3-\delta}$, which sinters rapidly (Figure 19e), the composite maintained its porosity (Figure 19f,g), highlighting the unique stabilizing ability of W^{6+} derived from the DP phase.[31]

5. Summary and Outlook

SOC electrode design is critical for performance and longevity. Composite materials are promising, but traditional preparation techniques hinder their full potential. In situ assembled composites provide a significant advantage as they allow us to control the nanostructure, distributing components more homogeneously, and enhancing interphase bonding. This review explores recent advancements in in situ assembled composite electrodes for SOCs, focusing on strategies for both fuel (metal exsolution and oxide segregation) and air (one-pot synthesis, segregation, phase reaction, and dynamic cation exchange) electrodes.

Developing in situ assembled composite catalysts for fuel electrodes has been predominantly centered around in situ metal exsolution and oxide segregation. In situ exsolved metal nanocatalysts typically exhibit a high specific surface area and strong bonding to the substrate. This translates to several advantages:

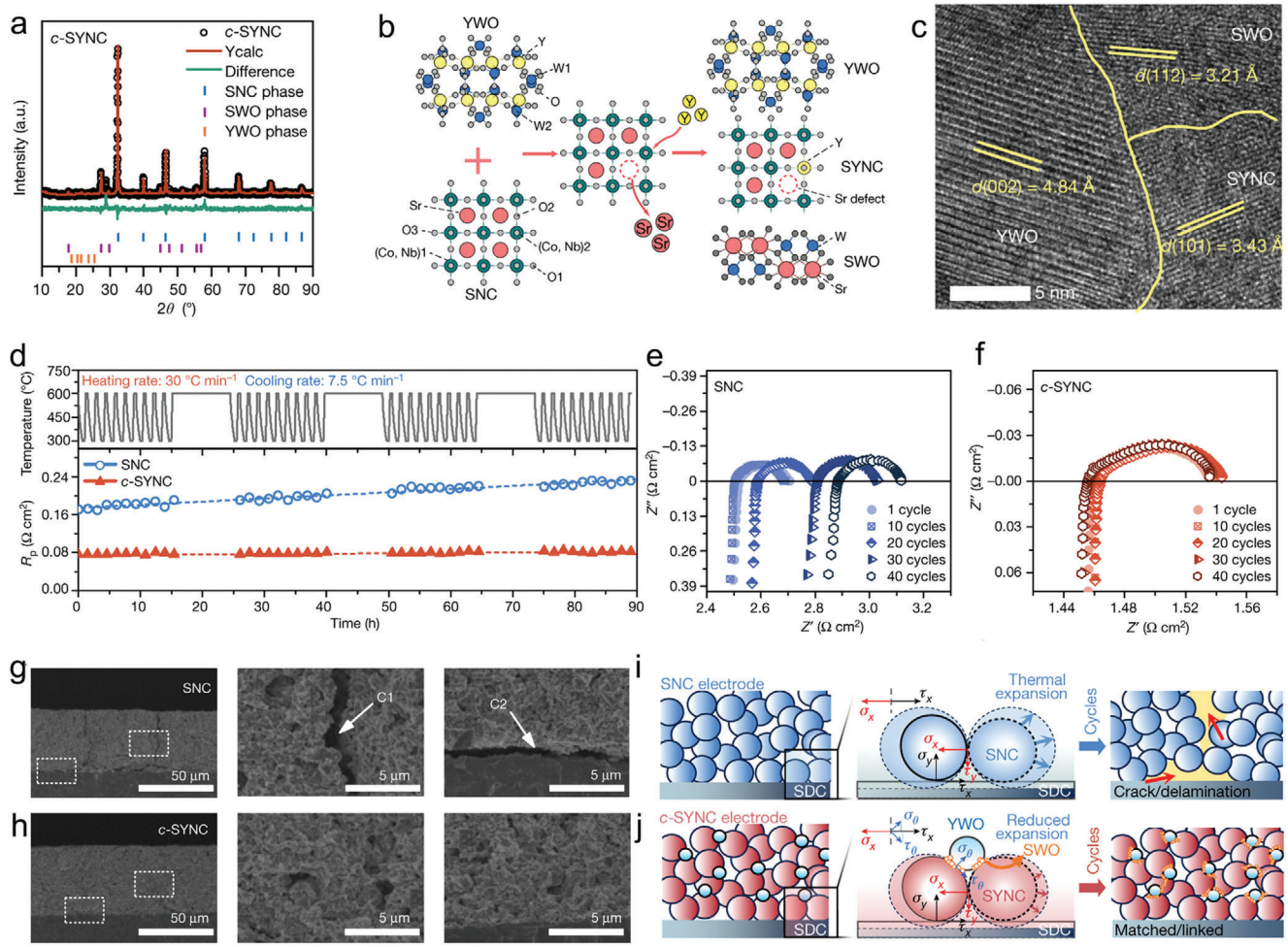

Figure 18. Characterization and performance of the *c*-SYNC composite electrode. a) Refined XRD pattern of *c*-SYNC. b) Schematic of the in situ assembled formation process. c) HRTEM image highlighting the interface between YWO, SWO, and SYNC phases. d) Polarization resistance comparison of symmetric cells with SNC and *c*-SYNC air electrodes over 40 thermal cycles (600 – 300 °C). EIS Nyquist plots for e) SNC-based and f) *c*-SYNC-based symmetric cells after cycling. Cross–section SEM images of symmetric cells after cycling: g) SNC and h) *c*-SYNC air electrodes. i,j) Schematic illustrating the mechanism of thermal expansion suppression in the *c*-SYNC composite electrode via thermal expansion offset. Reproduced with permission.[30] Copyright 2021, Springer Nature Limited.

more active sites for fuel reactions (boosting performance), along with better resistance to sintering, coking, and sulfur poisoning. Alloy nano-catalysts created by in situ exsolution share these benefits while offering additional synergies between the different metals and the supporting oxide. In situ oxide segregation, which is, in essence, oxidative metal exsolution, has also been shown to improve the activity and stability of fuel electrodes. Unlike typical metal exsolution, which disrupts the oxide crystal structure by creating defects, topotactic exsolution uniquely prevents the formation of these defects, thus preventing structural destabilization.

In situ assembled composites offer distinct advantages for air electrodes in SOCs. Their constituent phases provide the diverse properties required for SOC electrode functionality. Furthermore, in situ assembly creates a nanocomposite with close phase contact, maximizing the density of catalytic centers. Additionally, lattice interdiffusion between phases leads to strong adhesion, preventing sintering, mitigating thermal expansion, and ultimately improving electrode durability. Strategies for developing in situ assembled composite air electrode materials include one-pot synthesis, segregation, phase reaction, and dynamic cation exchange. One-pot synthesis has been used to make nanocomposites with nominal compositions SCFN[27] and BCCY.[52] These composites feature uniform phase distribution and strong interactions, resulting in bifunctionality, high activity, excellent thermal compatibility, and resistance to sintering. The exsolution/re-oxidation and segregation strategies favor the formation of surface-enriched nano-catalysts (such as Ag, NiO, CeO_2, $(La,Sr)CoO_{3-\delta}$, and $BaCoO_{3-\delta}$). These nano-catalysts modify the substrate and enhance crucial surface electrochemical processes like oxygen/steam adsorption and exchange. Phase reactions occur in two ways: cation exchange between phases or cation segregation followed by inter-reaction to form new phases. In the case of SNC and YWO, a unique phase reaction leads to an A-site deficient SYNC perovskite and SWO. SYNC's increased oxygen vacancies boost ORR activity,

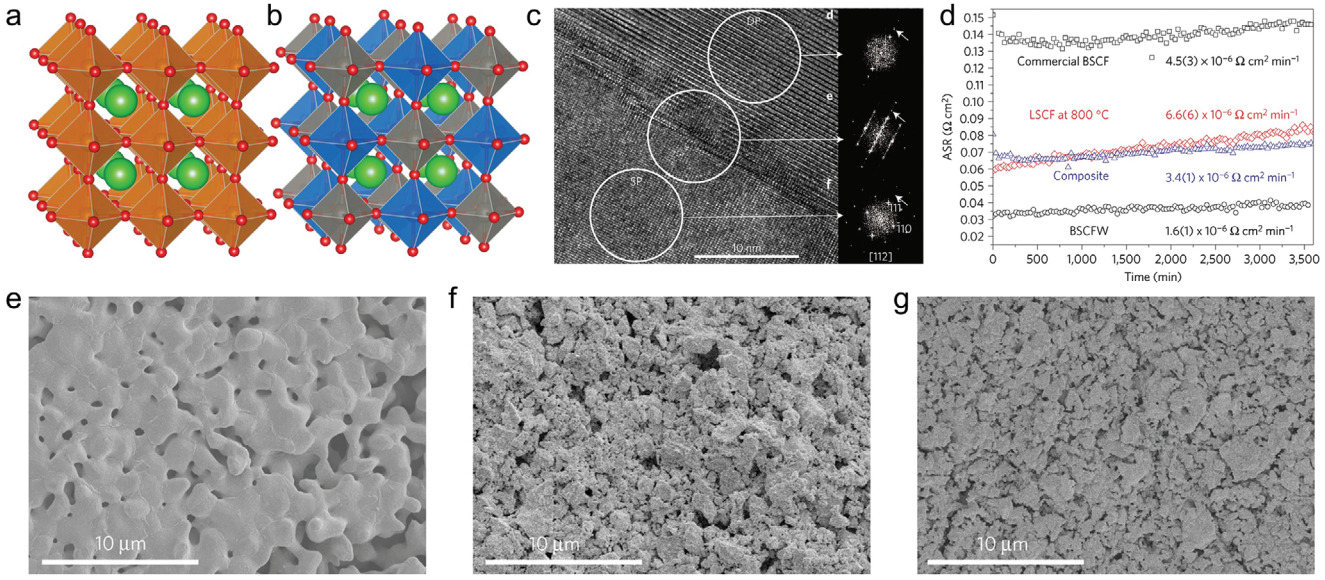

Figure 19. $Ba_{0.5}Sr_{0.5}(Co_{0.8}Fe_{0.2})_{0.6875}W_{0.3125}O_{3-\delta}$ electrode characterization and performance. a,b) Crystal structures of $Ba_{0.5}Sr_{0.5}Co_{0.589(10)}Fe_{0.354(9)}W_{0.056(3)}O_{2.304(21)}$ and $BaSrCo_{0.847(12)}Fe_{0.260(22)}W_{0.891(17)}O_6$ phases. c) HRTEM image of the interface between the two. d) Electrode resistance stability comparison highlights $Ba_{0.5}Sr_{0.5}(Co_{0.8}Fe_{0.2})_{0.6875}W_{0.3125}O_{3-\delta}$'s superiority over $Ba_{0.5}Sr_{0.5}Co_{0.8}Fe_{0.2}O_{3-\delta}$, $La_{0.6}Sr_{0.4}Co_{0.2}Fe_{0.8}O_{3-\delta}$, and $Ba_{0.5}Sr_{0.5}Co_{0.8}Fe_{0.2}O_{3-\delta}$+$BaSrCoWO_6$ composites. SEM images of e) $Ba_{0.5}Sr_{0.5}Co_{0.8}Fe_{0.2}O_{3-\delta}$, f) $Ba_{0.5}Sr_{0.5}(Co_{0.8}Fe_{0.2})_{0.6875}W_{0.3125}O_{3-\delta}$, g) $Ba_{0.5}Sr_{0.5}Co_{0.8}Fe_{0.2}O_{3-\delta}$+$BaSrCoWO_6$ electrode microstructures. Reproduced with permission.[31] Copyright 2017, Springer Nature Limited.

while SWO improves the SYNC-YWO connection, suppressing thermal expansion and enhancing durability. Finally, dynamic in situ assembly involves continuous cation exchange within the composite, simultaneously improving catalytic activity and durability.[30]

Although in situ assembled composites have shown promising activity, they present challenges that require further fundamental research. A key issue is the difficulty in determining the precise crystal properties of each phase, especially during SOC operation. For example, the SCFN composite consists of a primary SF-based perovskite (T-SCFN) and three minor phases, including RP-SCFN, and surface-enriched NiO and CeO_2. However, precisely quantifying and locating Ce and Ni dopants within the two perovskite phases remains difficult. This limitation forces researchers to model the T-SCFN and RP-SCFN perovskites with $Sr_8Fe_8O_{23}$ and $Sr_4Fe_3O_{10}$, respectively, for density functional theory calculations, potentially leading to results that deviate from actual operating conditions.[124] Advanced characterization techniques, including neutron powder diffraction, synchrotron X-ray absorption spectroscopy, aberration-corrected transmission electron microscopy, and energy-dispersive X-ray spectroscopy (EDS), are crucial for accurate analysis of phase species, structure, composition, and interface in situ assembled composites. In situ microscopy and spectroscopy can detect dynamic formation and transformation processes, providing valuable insights for computation and theoretical research.

In the context of SOCs, Ni-based fuel electrode-supported cells are nearing commercialization. Further research should concentrate on modifying these cermet electrodes by substitution and in situ exsolution strategies to enhance catalytic activity and ionic conductivity. Alloy exsolution could be a promising avenue for improving fuel oxidation, coke and sulfur resistance, and overall cell performance. A deeper understanding of nano-metal catalyst exsolution mechanisms, oxide segregation, and the role of exsolved nano-catalysts in fuel catalysis is crucial. Thorough theoretical and experimental studies should explore these areas.

Future air electrode research should focus on tailoring materials to the specific electrolyte (oxygen-ion or proton-conducting). For O-SOCs, optimizing oxygen-related properties (adsorption/desorption, dissociation, surface exchange, and bulk diffusion) is crucial. H-SOCs require attention to both oxygen and proton-related properties, including balancing oxygen surface exchange and bulk diffusion with strong hydration for proton conductivity. This balance is vital for maximizing cell efficiency and operational longevity.

Acknowledgements

Y.S. and Y.S. contributed equally to this work. The authors gratefully acknowledge the support of the Hong Kong Research Grant Council General Research Fund (16201820, 16201622) and Green Tech Fund (GTF202020131). This work was partly supported by the Project of Hetao Shenzhen-Hong Kong Science and Technology Innovation Cooperation Zone (HZQB-KCZYB-2020083).

Conflict of Interest

The authors declare no conflict of interest.

Keywords

electrodes, in situ assembly, nanocomposites, perovskites, solid oxide cells

Received: April 15, 2024
Revised: May 25, 2024
Published online: August 2, 2024

[1] P. Boldrin, N. P. Brandon, *Nat. Catal.* **2019**, *2*, 571.
[2] A. Hauch, R. Küngas, P. Blennow, A. B. Hansen, J. B. Hansen, B. V. Mathiesen, M. B. Mogensen, *Science* **2020**, *370*, eaba6118.
[3] C. Ni, J. Zhou, Z. Zhang, S. Li, J. Ni, K. Wu, J. T. S. Irvine, *Energy Environ. Sci.* **2021**, *14*, 6287.
[4] C. Su, W. Wang, M. Liu, M. O. Tadé, Z. Shao, *Adv. Energy Mater.* **2015**, *5*, 1500188.
[5] N. Wang, C. Tang, L. Du, R. Zhu, L. Xing, Z. Song, B. Yuan, L. Zhao, Y. Aoki, S. Ye, *Adv. Energy Mater.* **2022**, *12*, 2201882.
[6] W. Wang, C. Su, Y. Wu, R. Ran, Z. Shao, *Chem. Rev.* **2013**, *113*, 8104.
[7] Y. Zhang, R. Knibbe, J. Sunarso, Y. Zhong, W. Zhou, Z. Shao, Z. Zhu, *Adv. Mater.* **2017**, *29*, 1700132.
[8] A. Atkinson, S. Barnett, R. J. Gorte, J. T. S. Irvine, A. J. McEvoy, M. Mogensen, S. C. Singhal, J. Vohs, *Nat. Mater.* **2004**, *3*, 17.
[9] B. Morel, R. Roberge, S. Savoie, T. W. Napporn, M. Meunier, *Appl. Catal. A-Gen.* **2007**, *323*, 181.
[10] M. A. Haider, S. McIntosh, *J. Electrochem. Soc.* **2009**, *156*, B1369.
[11] C. Duan, J. Tong, M. Shang, S. Nikodemski, M. Sanders, S. Ricote, A. Almansoori, R. O'Hayre, *Science* **2015**, *349*, 1321.
[12] S. Choi, T. C. Davenport, S. M. Haile, *Energy Environ. Sci.* **2019**, *12*, 206.
[13] B. S. Prakash, S. S. Kumar, S. T. Aruna, *Renew. Sust. Energ. Rev.* **2014**, *36*, 149.
[14] J. Nielsen, J. Hjelm, *Electrochim. Acta* **2014**, *115*, 31.
[15] K. Sugihara, M. Asamoto, Y. Itagaki, T. Takemasa, S. Yamaguchi, Y. Sadaoka, H. Yahiro, *Solid State Ionics* **2014**, *262*, 433.
[16] D. Ding, X. Li, S. Y. Lai, K. Gerdes, M. Liu, *Energy Environ. Sci.* **2014**, *7*, 552.
[17] Y. Yin, S. Yu, H. Dai, L. Bi, *J. Mater. Chem. A* **2022**, *10*, 1726.
[18] C. Duan, R. J. Kee, H. Zhu, C. Karakaya, Y. Chen, S. Ricote, A. Jarry, E. J. Crumlin, D. Hook, R. Braun, N. P. Sullivan, R. O'Hayre, *Nature* **2018**, *557*, 217.
[19] Y. Li, Y. Li, M. Singh, Z. Li, X. Hu, L. Fan, *ACS Appl. Energy Mater.* **2022**, *5*, 14391.
[20] H. Bai, Y. Zhang, J. Chu, Q. Zhou, H. Lan, J. Zhou, *ACS Appl. Mater. Interfaces* **2023**, *15*, 38581.
[21] Q. Long, R. Sha, R. Wang, B. Xu, H. Men, Q. Wang, J. Hou, *Prog. Nat. Sci-Mater.* **2023**, *33*, 267.
[22] Y. Song, H. Li, M. Xu, G. Yang, W. Wang, R. Ran, W. Zhou, Z. Shao, *Small* **2020**, *16*, 2001859.
[23] D. Neagu, T. S. Oh, D. N. Miller, H. Ménard, S. M. Bukhari, S. R. Gamble, R. J. Gorte, J. M. Vohs, J. T. S. Irvine, *Nat. Commun.* **2015**, *6*, 8120.
[24] T. Zhu, H. E. Troiani, L. V. Mogni, M. Han, S. A. Barnett, *Joule* **2018**, *2*, 478.
[25] S. Joo, O. Kwon, K. Kim, S. Kim, H. Kim, J. Shin, H. Y. Jeong, S. Sengodan, J. W. Han, G. Kim, *Nat. Commun.* **2019**, *10*, 697.
[26] Y. Song, W. Wang, L. Ge, X. Xu, Z. Zhang, P. S. B. Julião, W. Zhou, Z. Shao, *Adv. Sci.* **2017**, *4*, 1700337.
[27] Y. Song, Y. Chen, M. Xu, W. Wang, Y. Zhang, G. Yang, R. Ran, W. Zhou, Z. Shao, *Adv. Mater.* **2020**, *32*, 1906979.
[28] G. Yang, W. Zhou, M. Liu, Z. Shao, *ACS Appl. Mater. Interfaces* **2016**, *8*, 35308.
[29] Y. Chen, S. Yoo, W. Zhang, J. H. Kim, Y. Zhou, K. Pei, N. Kane, B. Zhao, R. Murphy, Y. Choi, *ACS Catal.* **2019**, *9*, 7137.
[30] Y. Zhang, B. Chen, D. Guan, M. Xu, R. Ran, M. Ni, W. Zhou, R. O'Hayre, Z. Shao, *Nature* **2021**, *591*, 246.
[31] J. F. Shin, W. Xu, M. Zanella, K. Dawson, S. N. Savvin, J. B. Claridge, M. J. Rosseinsky, *Nat. Energy* **2017**, *2*, 16214.
[32] A. Choudhury, H. Chandra, A. Arora, *Renew. Sustain. Energy Rev.* **2013**, *20*, 430.
[33] C. Duan, J. Huang, N. Sullivan, R. O'Hayre, *Appl. Phys. Rev.* **2020**, *7*, 011314.
[34] J. Peng, J. Huang, X. Wu, Y. Xu, H. Chen, X. Li, *J. Power Sources* **2021**, *505*, 230058.
[35] S. A. Saadabadi, A. T. Thattai, L. Fan, R. E. F. Lindeboom, H. Spanjers, P. V. Aravind, *Renew. Energy* **2019**, *134*, 194.
[36] Y. Yang, Y. Zhang, M. Yan, *Sep. Purif. Technol.* **2022**, *298*, 121627.
[37] S. Hussain, Y. Li, *Energy Transit* **2020**, *4*, 113.
[38] A. Pesce, A. Hornés, M. Núñez, A. Morata, M. Torrell, A. Tarancón, *J. Mater. Chem. A* **2020**, *8*, 16926.
[39] K. Chen, *Int. J. Hydrogen Energy* **2011**, *36*, 10541.
[40] A. Ndubuisi, S. Abouali, K. Singh, V. Thangadurai, *J. Mater. Chem. A* **2022**, *10*, 2196.
[41] I. Setiawan, *J. Adv. Res. Fluid Mech. Therm. Sci.* **2021**, *82*, 39.
[42] H. Shi, C. Su, R. Ran, J. Cao, Z. Shao, *Prog. Nat. Sci-Mater.* **2020**, *30*, 764.
[43] J. Zhang, C. Lenser, N. H. Menzler, O. Guillon, *Solid State Ionics* **2020**, *344*, 115138.
[44] Z. Zeng, Y. Qian, Y. Zhang, C. Hao, D. Dan, W. Zhuge, *Appl. Energy* **2020**, *280*, 115899.
[45] V. V. Kharton, F. M. B. Marques, A. Atkinson, *Solid State Ionics* **2004**, *174*, 135.
[46] W. Zhang, Y. Zhou, E. Liu, Y. Ding, Z. Luo, T. Li, N. Kane, B. Zhao, Y. Niu, Y. Liu, *Appl. Catal. B-Environ.* **2021**, *299*, 120631.
[47] S. Zha, C. Xia, G. Meng, *J. Power Sources* **2003**, *115*, 44.
[48] M. Li, M. Zhao, F. Li, W. Zhou, V. K. Peterson, X. Xu, Z. Shao, I. Gentle, Z. Zhu, *Nat. Commun.* **2017**, *8*, 13990.
[49] Z. Shao, S. M. Haile, *Nature* **2004**, *431*, 170.
[50] W. Zhou, J. Sunarso, M. Zhao, F. Liang, T. Klande, A. Feldhoff, *Angew. Chem., Int. Ed.* **2013**, *52*, 14036.
[51] M. Chen, M. Zhou, Z. Liu, J. Liu, *Ceram. Int.* **2022**, *48*, 17208.
[52] Y. Song, Y. Chen, W. Wang, C. Zhou, Y. Zhong, G. Yang, W. Zhou, M. Liu, Z. Shao, *Joule* **2019**, *3*, 2842.
[53] F. He, M. Liang, W. Wang, R. Ran, G. Yang, W. Zhou, Z. Shao, *Energy Fuel* **2020**, *34*, 11464.
[54] H. Shimada, Y. Yamaguchi, H. Sumi, Y. Mizutani, *J. Electrochem. Soc.* **2020**, *167*, 124506.
[55] M. Choi, J. Paik, D. Kim, D. Woo, J. Lee, S. J. Kim, J. Lee, W. Lee, *Energy Environ. Sci.* **2021**, *14*, 6476.
[56] K. Hong, S. N. Sutanto, J. A. Lee, J. Hong, *J. Mater. Chem. A* **2021**, *9*, 6139.
[57] Y. Liu, S. Zha, M. Liu, *Adv. Mater.* **2004**, *16*, 256.
[58] J. H. Shim, S. Kang, S. W. Cha, W. Lee, Y. B. Kim, J. S. Park, T. M. Guer, F. B. Prinz, C. C. Chao, J. An, *J. Mater. Chem. A* **2013**, *1*, 12695.
[59] S. L. Zhang, T. Liu, C. J. Li, S. W. Yao, C. X. Li, G. J. Yang, M. Liu, *J. Mater. Chem. A* **2015**, *3*, 7535.
[60] P. Gannon, M. Deibert, P. White, R. Smith, H. Chen, W. Priyantha, J. Lucas, V. Gorokhovsky, *Int. J. Hydrogen Energy* **2008**, *33*, 3991.
[61] S. P. S. Shaikh, A. Muchtar, M. R. Somalu, *Renew. Sustain. Energy Rev.* **2015**, *51*, 1.
[62] J. I. Lee, K. Y. Park, H. Park, H. Bae, M. Saqib, K. Park, J. S. Shin, M. Jo, J. Kim, S. J. Song, *J. Power Sources* **2021**, *510*, 230409.
[63] H. Cai, L. Zhang, J. Xu, J. Huang, X. Wei, L. Wang, Z. Song, W. Long, *Electrochim. Acta* **2019**, *320*, 134642.
[64] Y. Kalinci, I. Dincer, *Int. J. Hydrogen Energy* **2018**, *43*, 5795.
[65] P. Marocco, D. Ferrero, A. Lanzini, M. Santarelli, *Appl. Energy* **2019**, *241*, 472.
[66] O. Costa-Nunes, R. J. Gorte, J. M. Vohs, *J. Power Sources* **2005**, *141*, 241.

[67] L. Zhu, C. Cadigan, C. Duan, J. Huang, L. Bian, L. Le, C. H. Hernandez, V. Avance, R. O'Hayre, N. P. Sullivan, *Commun. Chem.* **2021**, *4*, 121.
[68] Y. Wang, J. Yang, J. Wang, W. Guan, B. Chi, L. Jia, H. Ying, Y. Xia, J. Chen, *ECS Trans.* **2019**, *91*, 1611.
[69] Y. Pan, H. Zhang, K. Xu, Y. Zhou, B. Zhao, W. Yuan, K. Sasaki, Y. Choi, Y. Chen, M. Liu, *Appl. Catal. B-Environ.* **2022**, *306*, 121071.
[70] S. K. Kim, S. H. Hwang, J. T. Nam, J. S. Park, *J. Power Sources* **2021**, *513*, 230544.
[71] G. Herz, E. Reichelt, M. Jahn, *Appl. Energy* **2018**, *215*, 309.
[72] P. K. Addo, B. Molero-Sanchez, M. Chen, S. Paulson, V. Birss, *Fuel cells* **2015**, *15*, 689.
[73] F. N. Cayan, M. Zhi, S. R. Pakalapati, I. Celik, N. Wu, R. Gemmen, *J. Power Sources* **2008**, *185*, 595.
[74] N. Bausa, S. Escolastico, J. M. Serra, *J. CO2 Util.* **2019**, *34*, 231.
[75] J. Sarabut, S. Charojrochkul, T. Sornchamni, N. Laosiripojana, S. Assabumrungrat, U. Wetwatana-Hartley, P. Kim-Lohsoontorn, *Int. J. Hydrogen Energy* **2019**, *44*, 20634.
[76] S. Huang, C. Yang, H. Chen, N. Zhou, D. Tucker, *Case Stud. Therm. Eng.* **2022**, *31*, 101868.
[77] S. Campanari, L. Mastropasqua, M. Gazzani, P. Chiesa, M. C. Romano, *J. Power Sources* **2016**, *325*, 194.
[78] M. Beigzadeh, F. Pourfayaz, M. H. Ahmadi, S. M. Pourkiaei, M. Beigzadeh, *Fuel Cells* **2017**, *17*, 843.
[79] S. Y. Gómez, D. Hotza, *Renew. Sustain. Energy Rev.* **2016**, *61*, 155.
[80] M. B. Mogensen, M. Chen, H. L. Frandsen, C. Graves, J. B. Hansen, K. V. Hansen, A. Hauch, T. Jacobsen, S. H. Jensen, T. L. Skafte, *Clean Energy* **2019**, *3*, 175.
[81] W. Yue, Y. Li, Y. Zheng, T. Wu, C. Zhao, J. Zhao, G. Geng, W. Zhang, J. Chen, J. Zhu, *Nano Energy* **2019**, *62*, 883.
[82] Z. Wang, Y. Li, J. W. Schwank, *J. Power Sources* **2014**, *248*, 239.
[83] E. Ioannidou, C. Neofytidis, L. Sygellou, D. K. Niakolas, *Appl. Catal. B-Environ.* **2018**, *236*, 253.
[84] E. Pikalova, D. Medvedev, *Int. J. Hydrogen Energy* **2016**, *41*, 4016.
[85] N. Nasani, D. Ramasamy, I. Antunes, J. Perez, D. P. Fagg, *Electrochim. Acta* **2015**, *154*, 387.
[86] Y. Kuru, M. Wohlschlögel, U. Welzel, E. J. Mittemeijer, *Appl. Phys. Lett.* **2007**, *90*, 243113.
[87] X. Y. Liu, Z. H. Xu, G. Y. Liang, *Mater. Lett.* **2017**, *191*, 108.
[88] Z. Zhu, M. Zhou, K. Tan, Z. Fan, D. Cao, Z. Liu, M. Chen, Y. Chen, M. Chen, J. Liu, *ACS Appl. Mater. Interfaces* **2023**, *15*, 14457.
[89] P. Boldrin, E. Ruiz-Trejo, J. Mermelstein, J. M. Bermudez Menendez, T. s. Ramirez Reina, N. P. Brandon, *Chem. Rev.* **2016**, *116*, 13633.
[90] D. Sarantaridis, A. Atkinson, *Fuel cells* **2007**, *7*, 246.
[91] Z. Liu, M. Zhou, M. Chen, D. Cao, J. Shao, M. Liu, J. Liu, *Ceram. Int.* **2020**, *46*, 19952.
[92] Y. Song, W. Wang, J. Qu, Y. Zhong, G. Yang, W. Zhou, Z. Shao, *ACS Appl. Mater. Interfaces* **2018**, *10*, 41257.
[93] Y. Zou, T. Lin, Y. Sun, Z. Chen, C. Guan, Y. Li, N. Ai, K. Chen, *Electrochim. Acta* **2021**, *391*, 138912.
[94] D. H. Prasad, H. I. Ji, H. R. Kim, J. W. Son, B. K. Kim, H. W. Lee, J. H. Lee, *Appl. Catal. B-Environ.* **2011**, *101*, 531.
[95] H. Takahashi, T. Takeguchi, N. Yamamoto, M. Matsuda, E. Kobayashi, W. Ueda, *J. Mol. Catal. A-Chem.* **2011**, *350*, 69.
[96] M. Shishkin, T. Ziegler, *ECS Trans.* **2011**, *35*, 1611.
[97] W. Wang, R. Ran, C. Su, Y. Guo, D. Farrusseng, Z. Shao, *J. Power Sources* **2013**, *240*, 232.
[98] Z. Cheng, J. H. Wang, Y. Choi, L. Yang, M. C. Lin, M. Liu, *Energy Environ. Sci.* **2011**, *4*, 4380.
[99] H. Kishimoto, T. Horita, K. Yamaji, M. E. Brito, Y. Xiong, H. Yokokawa, *J. Electrochem. Soc.* **2010**, *157*, B802.
[100] M. Riegraf, G. Schiller, R. Costa, K. A. Friedrich, A. Latz, V. Yurkiv, *J. Electrochem. Soc.* **2014**, *162*, F65.
[101] D. Papurello, A. Lanzini, S. Fiorilli, F. Smeacetto, R. Singh, M. Santarelli, *Chem. Eng. J.* **2016**, *283*, 1224.
[102] T. Yoshizumi, S. Taniguchi, Y. Shiratori, K. Sasaki, *J. Electrochem. Soc.* **2012**, *159*, F693.
[103] L. Yang, Z. Cheng, M. Liu, L. Wilson, *Energy Environ. Sci.* **2010**, *3*, 1804.
[104] D. K. Niakolas, *Appl. Catal. A-Gen.* **2014**, *486*, 123.
[105] W. H. Kan, V. Thangadurai, *Ionics* **2015**, *21*, 301.
[106] J. B. Goodenough, Y. H. Huang, *J. Power Sources* **2007**, *173*, 1.
[107] S. K. Burnwal, S. Bharadwaj, P. Kistaiah, *J. Mol. Eng. Mater.* **2016**, *4*, 1630001.
[108] S. P. Jiang, *Int. J. Hydrogen Energy* **2019**, *44*, 7448.
[109] L. Shu, J. Sunarso, S. S. Hashim, J. Mao, W. Zhou, F. Liang, *Int. J. Hydrogen Energy* **2019**, *44*, 31275.
[110] I. Z. Rahman, M. A. Raza, M. A. Rahman, *Adv. Mater. Res.* **2012**, *445*, 497.
[111] J. W. Fergus, *Solid State Ionics* **2006**, *177*, 1529.
[112] M. Chen, S. Paulson, V. Thangadurai, V. Birss, *J. Power Sources* **2013**, *236*, 68.
[113] P. I. Cowin, C. T. G. Petit, R. Lan, J. T. S. Irvine, S. Tao, *Adv. Energy Mater.* **2011**, *1*, 314.
[114] D. N. Miller, J. T. S. Irvine, *J. Power Sources* **2011**, *196*, 7323.
[115] A. Vincent, J. L. Luo, K. T. Chuang, A. R. Sanger, *J. Power Sources* **2010**, *195*, 769.
[116] T. Zhu, H. Troiani, L. V. Mogni, M. Santaya, M. Han, S. A. Barnett, *J. Power Sources* **2019**, *439*, 227077.
[117] D. E. Fowler, A. C. Messner, E. C. Miller, B. W. Slone, S. A. Barnett, K. R. Poeppelmeier, *Chem. Mater.* **2015**, *27*, 3683.
[118] C. Aliotta, L. F. Liotta, F. Deganello, V. La Parola, A. Martorana, *Appl. Catal. B-Environ.* **2016**, *180*, 424.
[119] Y. F. Sun, J. H. Li, M. N. Wang, B. Hua, J. Li, J. L. Luo, *J. Mater. Chem. A* **2015**, *3*, 14625.
[120] M. S. Khan, X. Xu, R. Knibbe, Z. Zhu, *Renew. Sustain. Energy Rev.* **2021**, *143*, 110918.
[121] L. Bi, S. Boulfrad, E. Traversa, *Chem. Soc. Rev.* **2014**, *43*, 8255.
[122] S. J. Kim, K. J. Kim, A. M. Dayaghi, G. M. Choi, *Int. J. Hydrogen Energy* **2016**, *41*, 14498.
[123] H. Ding, W. Wu, C. Jiang, Y. Ding, W. Bian, B. Hu, P. Singh, C. J. Orme, L. Wang, Y. Zhang, *Nat. Commun.* **2020**, *11*, 1907.
[124] Y. Song, J. Liu, Y. Wang, D. Guan, A. Seong, M. Liang, M. J. Robson, X. Xiong, Z. Zhang, G. Kim, Z. Shao, F. Ciucci, *Adv. Energy Mater.* **2021**, *11*, 2101899.
[125] A. Jun, J. Kim, J. Shin, G. Kim, *ChemElectroChem* **2016**, *3*, 511.
[126] J. Xu, C. Chen, Z. Han, Y. Yang, J. Li, Q. Deng, *Nanomaterials* **2019**, *9*, 1161.
[127] C. Sun, R. Hui, J. Roller, *J. Solid State Electrochem.* **2010**, *14*, 1125.
[128] D. Rembelski, J. P. Viricelle, L. Combemale, M. Rieu, *Fuel Cells* **2012**, *12*, 256.
[129] G. Chen, Y. Gao, Y. Luo, R. Guo, *Ceram. Int.* **2017**, *43*, 1304.
[130] D. P. Tarragó, B. Moreno, E. Chinarro, C. de Fraga Malfatti, V. C. de Sousa, *Int. J. Hydrogen Energy* **2020**, *45*, 11749.
[131] W. Zhang, H. Yun, *Catal. Today* **2023**, *409*, 71.
[132] R. V. Kumar, A. P. Khandale, *Renew. Sustain. Energy Rev.* **2022**, *156*, 111985.
[133] N. A. Baharuddin, A. Muchtar, M. R. Somalu, *Int. J. Hydrogen Energy* **2017**, *42*, 9149.
[134] S. S. Hashim, F. Liang, W. Zhou, J. Sunarso, *ChemElectroChem* **2019**, *6*, 3549.
[135] M. A. Azimova, S. McIntosh, *Solid State Ionics* **2011**, *203*, 57.
[136] A. Grimaud, F. Mauvy, J. M. Bassat, S. Fourcade, L. Rocheron, M. Marrony, J. C. Grenier, *J. Electrochem. Soc.* **2012**, *159*, B683.
[137] S. Li, K. Xie, *J. Electrochem. Soc.* **2013**, *160*, F224.
[138] S. Sun, Z. Cheng, *J. Electrochem. Soc.* **2017**, *164*, F3104.

[139] H. An, H. W. Lee, B. K. Kim, J. W. Son, K. J. Yoon, H. Kim, D. Shin, H. I. Ji, J. H. Lee, *Nat. Energy* **2018**, *3*, 870.
[140] R. Ren, Z. Wang, X. Meng, X. Wang, C. Xu, J. Qiao, W. Sun, K. Sun, *ACS Appl. Energy Mater.* **2020**, *3*, 4914.
[141] T. Gan, X. Fan, Y. Liu, C. Wang, H. Mei, L. Fan, N. Hou, Y. Zhao, Y. Li, *J. Mater. Chem. A* **2020**, *8*, 7792.
[142] Y. Song, J. Chen, M. Yang, M. Xu, D. Liu, M. Liang, Y. Wang, R. Ran, W. Wang, F. Ciucci, Z. Shao, *Small* **2022**, *18*, 2200450.
[143] T. Yang, J. Liu, Y. Lei, W. Li, T. L. Cheng, H. Finklea, Y. H. Wen, X. Liu, H. W. Abernathy, S. Lee, T. L. Kalapos, G. A. Hackett, *J. Electrochem. Soc.* **2019**, *166*, F448.
[144] S. Tafaroji, M. Farbod, I. Kazeminezhad, M. Kheirmand, *Mater. Res. Express* **2019**, *6*, 095522.
[145] H. Lee, H. Jung, C. Kim, S. Kim, I. Jang, H. Yoon, U. Paik, T. Song, *ACS Appl. Energy Mater.* **2021**, *4*, 11564.
[146] P. Keyvanfar, A. R. Hanifi, P. Sarkar, T. H. Etsell, V. Birss, *ECS Trans.* **2015**, *68*, 1255.
[147] S. Sengodan, M. Liu, T. H. Lim, J. Shin, M. Liu, G. Kim, *J. Electrochem. Soc.* **2014**, *161*, F668.
[148] X. Lou, S. Wang, Z. Liu, L. Yang, M. Liu, *Solid State Ionics* **2009**, *180*, 1285.
[149] Y. Li, W. Zhang, T. Wu, Y. Zheng, J. Chen, B. Yu, J. Zhu, M. Liu, *Adv. Energy Mater.* **2018**, *8*, 1801893.
[150] Y. Gao, J. Wang, Y. Q. Lyu, K. Lam, F. Ciucci, *J. Mater. Chem. A* **2017**, *5*, 6399.
[151] Y. Gao, D. Chen, M. Saccoccio, Z. Lu, F. Ciucci, *Nano Energy* **2016**, *27*, 499.
[152] D. Neagu, V. Kyriakou, I. L. Roiban, M. Aouine, C. Tang, A. Caravaca, K. Kousi, I. Schreur-Piet, I. S. Metcalfe, P. Vernoux, *ACS Nano* **2019**, *13*, 12996.
[153] J. H. Kim, J. K. Kim, J. Liu, A. Curcio, J. S. Jang, I. D. Kim, F. Ciucci, W. Jung, *ACS Nano* **2020**, *15*, 81.
[154] Z. Du, H. Zhao, S. Yi, Q. Xia, Y. Gong, Y. Zhang, X. Cheng, Y. Li, L. Gu, K. Swierczek, *ACS Nano* **2016**, *10*, 8660.
[155] X. Chen, W. Ni, J. Wang, Q. Zhong, M. Han, T. Zhu, *Electrochim. Acta* **2018**, *277*, 226.
[156] S. Sengodan, Y. W. Ju, O. Kwon, A. Jun, H. Y. Jeong, T. Ishihara, J. Shin, G. Kim, *ACS Sustainable Chem. Eng.* **2017**, *5*, 9207.
[157] Z. Liu, Y. Chen, G. Yang, M. Yang, R. Ji, Y. Song, R. Ran, W. Zhou, Z. Shao, *Appl. Catal. B-Environ.* **2022**, *319*, 121929.
[158] M. Wu, X. Zhou, J. Xu, S. Li, L. Pan, N. Zhang, *J. Power Sources* **2020**, *451*, 227334.
[159] Z. Zhang, J. Wang, Y. Chen, S. Tan, Z. Shao, D. Chen, *J. Power Sources* **2018**, *385*, 76.
[160] J. Shen, Y. Chen, G. Yang, W. Zhou, M. O. Tadé, Z. Shao, *J. Power Sources* **2016**, *306*, 92.
[161] G. Yang, C. Su, Y. Chen, M. O. Tade, Z. Shao, *J. Mater. Chem. A* **2014**, *2*, 19526.
[162] H. Gu, J. Sunarso, G. Yang, C. Zhou, Y. Song, Y. Zhang, W. Wang, R. Ran, W. Zhou, Z. Shao, *ACS Appl. Mater. Interfaces* **2020**, *12*, 16417.
[163] Y. Liu, L. Jia, J. Li, B. Chi, J. Pu, J. Li, *Compos. Part B-Eng.* **2020**, *193*, 108033.
[164] J. Zhao, Y. Pu, L. Li, W. Zhou, Y. Guo, *Energy Fuel* **2020**, *34*, 10100.
[165] X. Xi, Z. S. Cao, X. Q. Shen, Y. Lu, J. Li, J. L. Luo, X. Z. Fu, *J. Power Sources* **2020**, *459*, 228071.
[166] L. Thommy, M. Benamira, T. Jardiel, V. Günes, O. Joubert, M. T. Caldes, *Mater. Chem. Phys.* **2021**, *268*, 124724.
[167] F. Kosaka, T. Nakamura, J. Otomo, *J. Electrochem. Soc.* **2017**, *164*, F1323.
[168] P. B. Managutti, S. Tymen, X. Liu, O. Hernandez, C. Prestipino, A. Le Gal La Salle, S. Paul, L. Jalowiecki-Duhamel, V. Dorcet, A. Billard, *ACS Appl. Mater. Interfaces* **2021**, *13*, 35719.
[169] B. D. Madsen, W. Kobsiriphat, Y. Wang, L. D. Marks, S. Barnett, *ECS Trans.* **2007**, *7*, 1339.
[170] O. Kwon, S. Sengodan, K. Kim, G. Kim, H. Y. Jeong, J. Shin, Y. W. Ju, J. W. Han, G. Kim, *Nat. Commun.* **2017**, *8*, 15967.
[171] C. Xu, W. Sun, R. Ren, X. Yang, M. Ma, J. Qiao, Z. Wang, S. Zhen, K. Sun, *Appl. Catal. B-Environ.* **2021**, *282*, 119553.
[172] H. Qi, T. Yang, W. Li, L. Ma, S. Hu, W. Shi, E. M. Sabolsky, J. W. Zondlo, R. Hart, G. A. Hackett, *ECS Trans.* **2019**, *91*, 1701.
[173] N. Zhou, Y. M. Yin, Z. Chen, Y. Song, J. Yin, D. Zhou, Z. F. Ma, *J. Electrochem. Soc.* **2018**, *165*, F629.
[174] S. Park, Y. Kim, H. Han, Y. S. Chung, W. Yoon, J. Choi, W. B. Kim, *Appl. Catal. B-Environ.* **2019**, *248*, 147.
[175] V. Kyriakou, D. Neagu, E. I. Papaioannou, I. S. Metcalfe, M. C. M. van de Sanden, M. N. Tsampas, *Appl. Catal. B-Environ.* **2019**, *258*, 117950.
[176] C. Duan, R. J. Kee, H. Zhu, C. Karakaya, Y. Chen, S. Ricote, A. Jarry, E. J. Crumlin, D. Hook, R. Braun, *Nature* **2018**, *557*, 217.
[177] M. Qin, T. Tan, K. Li, Z. Wang, H. Yang, Z. Liu, M. Zhou, T. Liu, C. Yang, M. Liu, *Int. J. Hydrogen Energy* **2020**, *45*, 21464.
[178] R. Glaser, T. Zhu, H. Troiani, A. Caneiro, L. Mogni, S. Barnett, *J. Mater. Chem. A* **2018**, *6*, 5193.
[179] H. Lv, L. Lin, X. Zhang, D. Gao, Y. Song, Y. Zhou, Q. Liu, G. Wang, X. Bao, *J. Mater. Chem. A* **2019**, *7*, 11967.
[180] Y. Tian, Y. Liu, A. Naden, L. Jia, M. Xu, W. Cui, B. Chi, J. Pu, J. T. S. Irvine, J. Li, *J. Mater. Chem. A* **2020**, *8*, 14895.
[181] W. Zhang, H. Wang, K. Guan, J. Meng, Z. Wei, X. Liu, J. Meng, *ACS Appl. Mater. Interfaces* **2019**, *12*, 461.
[182] K. Y. Lai, A. Manthiram, *Chem. Mater.* **2018**, *30*, 2838.
[183] N. Hou, T. Yao, P. Li, X. Yao, T. Gan, L. Fan, J. Wang, X. Zhi, Y. Zhao, Y. Li, *ACS Appl. Mater. Interfaces* **2019**, *11*, 6995.
[184] Z. Teng, Z. Xiao, G. Yang, L. Guo, X. Yang, R. Ran, W. Wang, W. Zhou, Z. Shao, *Mater. Today Energy* **2020**, *17*, 100458.
[185] S. Liu, K. T. Chuang, J. L. Luo, *ACS Catal.* **2016**, *6*, 760.
[186] R. Thalinger, M. Gocyla, M. Heggen, B. Klötzer, S. Penner, *J. Phys. Chem. C* **2015**, *119*, 22050.
[187] J. Li, B. Wei, Z. Cao, X. Yue, Y. Zhang, Z. Lü, *ChemSusChem* **2018**, *11*, 254.
[188] Z. Wang, Y. M. Yin, Y. Yu, Y. Song, Z. F. Ma, J. Yin, *Int. J. Hydrogen Energy* **2018**, *43*, 10440.
[189] H. Lv, T. Liu, X. Zhang, Y. Song, H. Matsumoto, N. Ta, C. Zeng, G. Wang, X. Bao, *Angew. Chem., Int. Ed.* **2020**, *59*, 15968.
[190] Z. Yang, C. Ma, N. Wang, X. Jin, C. Jin, S. Peng, *J. CO2 Util.* **2019**, *33*, 445.
[191] S. Liu, Q. Liu, J. L. Luo, *ACS Catal.* **2016**, *6*, 6219.
[192] Y. Li, B. Hu, C. Xia, W. Q. Xu, J. P. Lemmon, F. Chen, *J. Mater. Chem. A* **2017**, *5*, 20833.
[193] B. Niu, C. Lu, W. Yi, S. Luo, X. Li, X. Zhong, X. Zhao, B. Xu, *Appl. Catal. B-Environ.* **2020**, *270*, 118842.
[194] Y. Guo, S. Wang, R. Li, J. Yu, X. Zhang, M. Li, X. Zheng, J. Zhu, Y. Song, G. Wang, *Joule* **2024**, *8*, https://doi.org/10.1016/j.joule.2024.04.009.
[195] F. Liu, H. Deng, Z. Wang, A. M. Hussain, N. Dale, Y. Furuya, Y. Miura, Y. Fukuyama, H. Ding, B. Liu, *J. Am. Chem. Soc.* **2024**, *146*, 4704.
[196] P. Qiu, X. Yang, W. Wang, T. Wei, Y. Lu, J. Lin, Z. Yuan, L. Jia, J. Li, F. Chen, *ACS Appl. Mater. Interfaces* **2020**, *12*, 13988.
[197] Y. F. Sun, J. H. Li, L. Cui, B. Hua, S. H. Cui, J. Li, J. L. Luo, *Nanoscale* **2015**, *7*, 11173.
[198] B. Li, S. He, J. Li, X. Yue, J. T. S. Irvine, D. Xie, J. Ni, C. Ni, *ACS Catal.* **2020**, *10*, 14398.
[199] J. Zhu, W. Zhang, Y. Li, W. Yue, G. Geng, B. Yu, *Appl. Catal. B-Environ.* **2020**, *268*, 118389.
[200] B. W. Zhang, M. N. Zhu, M. R. Gao, X. Xi, N. Duan, Z. Chen, R. F. Feng, H. Zeng, J. L. Luo, *Nature Commun* **2022**, *13*, 4618.
[201] H. Gu, G. Yang, Y. Hu, M. Liang, S. Chen, R. Ran, M. Xu, W. Wang, W. Zhou, Z. Shao, *Int. J. Hydrogen Energy* **2020**, *45*, 25996.

[202] Y. Chen, Y. Choi, S. Yoo, Y. Ding, R. Yan, K. Pei, C. Qu, L. Zhang, I. Chang, B. Zhao, *Joule* **2018**, *2*, 938.
[203] X. Li, Z. Jin, C. Wang, R. Peng, Y. Zha, J. Cao, Y. Ji, Z. Shao, *Adv. Energy Mater.* **2024**, *14*, 2400319.
[204] Z. Zhao, J. Cui, M. Zou, S. Mu, H. Huang, Y. Meng, K. He, K. S. Brinkman, J. J. Tong, *J. Power Sources* **2020**, *450*, 227609.
[205] J. H. Kim, J. K. Kim, H. G. Seo, D. K. Lim, S. J. Jeong, J. Seo, J. Kim, W. Jung, *Adv. Funct. Mater.* **2020**, *30*, 2001326.
[206] Y. Zhu, W. Zhou, R. Ran, Y. Chen, Z. Shao, M. Liu, *Nano Lett.* **2016**, *16*, 512.
[207] J. A. Farmer, C. T. Campbell, *Science* **2010**, *329*, 933.
[208] J. A. Farmer, J. H. Baricuatro, C. T. Campbell, *J. Phys. Chem. C* **2010**, *114*, 17166.
[209] C. T. Campbell, J. R. V. Sellers, *Faraday Discuss.* **2013**, *162*, 9.
[210] R. L. Cook, A. F. Sammells, *Solid State Ionics* **1991**, *45*, 311.
[211] A. Cao, R. Lu, G. Veser, *Phys. Chem. Chem. Phys.* **2010**, *12*, 13499.
[212] C. T. Campbell, C. H. F. Peden, *Science* **2005**, *309*, 713.
[213] J. W. Han, B. Yildiz, *Energy Environ. Sci.* **2012**, *5*, 8598.
[214] J. W. Han, B. Yildiz, *J. Mater. Chem.* **2011**, *21*, 18983.
[215] T. Hong, M. Zhao, K. Brinkman, F. Chen, C. Xia, *ACS Appl. Mater. Interfaces* **2017**, *9*, 8659.
[216] Y. Chen, S. Yoo, K. Pei, D. Chen, L. Zhang, B. deGlee, R. Murphy, B. Zhao, Y. Zhang, Y. Chen, *Adv. Funct. Mater.* **2018**, *28*, 1704907.
[217] J. H. Kim, S. Yoo, R. Murphy, Y. Chen, Y. Ding, K. Pei, B. Zhao, G. Kim, Y. Choi, M. Liu, *Energy Environ. Sci.* **2021**, *14*, 1506.
[218] K. Pei, Y. Zhou, K. Xu, H. Zhang, Y. Ding, B. Zhao, W. Yuan, K. Sasaki, Y. Choi, Y. Chen, *Nat. Commun.* **2022**, *13*, 2207.
[219] K. Xu, H. Zhang, Y. Xu, F. He, Y. Zhou, Y. Pan, J. Ma, B. Zhao, W. Yuan, Y. Chen, *Adv. Funct. Mater.* **2022**, *32*, 2110998.
[220] J. H. Kim, J. Hong, D. K. Lim, S. Ahn, J. Kim, J. K. Kim, D. Oh, S. Jeon, S. J. Song, W. Jung, *Energy Environ. Sci.* **2022**, *15*, 1097.
[221] K. Park, M. Saqib, H. Lee, D. Shin, M. Jo, K. M. Park, M. Hamayun, S. H. Kim, S. Kim, K. S. Lee, *Energy Environ. Sci.* **2024**, *17*, 1175.
[222] J. Zhang, Y. Ye, B. Wei, F. Hu, L. Sui, H. Xiao, L. Gui, J. Sun, B. He, L. Zhao, *Appl. Catal. B-Environ.* **2023**, *330*, 122661.
[223] Y. Lin, R. Ran, C. Zhang, R. Cai, Z. Shao, *J. Phys. Chem. A* **2010**, *114*, 3764.
[224] L. Yang, C. Zuo, S. Wang, Z. Cheng, M. Liu, *Adv. Mater.* **2008**, *20*, 3280.
[225] Y. Chen, J. Shen, G. Yang, W. Zhou, Z. Shao, *J. Mater. Chem. A* **2017**, *5*, 24842.

Yufei Song received his Ph.D. in Chemical Engineering from Nanjing Tech University in 2020. He is currently a Postdoctoral Fellow working with Prof. Francesco Ciucci at The Hong Kong University of Science and Technology, China. His research interests focus on the design and synthesis of perovskite-based oxides and their applications in intermediate and low-temperature solid oxide fuel cells.

Yixiao Song received his bachelor's degree from Henan University in 2022. He is currently a master's student in Chemical Engineering from Nanjing Tech University. His research interests focus on the design and development of electrode materials for reversible solid oxide cells.

Zongping Shao is a professor at Curtin University. He obtained his Ph.D. from the Dalian Institute of Chemical Physics, China in 2000. He worked as a visiting scholar at Institut de Researches Sur La Catalyse, CNRS, France, and as a postdoc at California Institute of Technology, USA from 2000 to 2005. His research interests include mixed conducting membranes for oxygen permeation, solid oxide fuel cells, room-temperature electrocatalysts, and advanced energy storage devices including lithium/sodium-(ion) batteries, metal-air batteries, supercapacitors, and solar cells. He has published >800 international journal papers with a total citation of >73,000 and an H-index of 131 (Google Scholar). He was selected as one of the highly cited researchers (2014, 2017–2024) by Clarivate Analytics.

Francesco Ciucci is the Chair of Electrode Design for Electrochemical Energy at the University of Bayreuth. He holds a Ph.D. from the California Institute of Technology and was formerly with the Hong Kong University of Science and Technology. Professor Ciucci's research centers on solid-state energy technologies, such as solid oxide fuel cells, electrolyzers, and batteries. He specializes in modeling these systems and developing advanced functional materials.